Ca^{2+} release via $InsP_3Rs$ enhances RyR recruitment during Ca^{2+} transients by increasing dyadic $[Ca^{2+}]$ in cardiomyocytes

Short title: Dyadic Ca^{2+} regulation by $InsP_3$

Kateryna Demydenko[1], Karin R. Sipido[1] and H. Llewelyn Roderick[1,*]

[1] KU Leuven, Department of Cardiovascular Sciences, Laboratory of Experimental Cardiology, B-3000, Leuven.

* For correspondence:

Prof Llewelyn Roderick, PhD

Laboratory of Experimental Cardiology

Department of Cardiovascular Sciences

CDG 9th Floor

KU Leuven

Campus Gasthuisberg

Herestraat 49

B-3000 Leuven

Belgium

E-mail: llewelyn.roderick@kuleuven.be

Key words: cardiac excitation-contraction coupling, $InsP_3R$, RyR, Ca^{2+} microdomains, Ca^{2+} release, Ca^{2+} sparks/nanosparks

Summary: Using a targeted Ca^{2+} reporter, signaling from dyadic $InsP_3Rs$ to co-located RyR channels is shown to augment sarcoplasmic Ca^{2+} release during excitation-contraction coupling in cardiomyocytes.

Abstract

Excitation-contraction coupling (ECC) relies on temporally synchronized sarcoplasmic reticulum (SR) Ca^{2+} release via ryanodine receptors (RyRs) at dyadic membrane compartments. Neurohormones, such as endothelin-1 (ET-1), that act via $G\alpha_q$-coupled G protein-coupled receptors (GPCRs) modulate Ca^{2+} dynamics during ECC and induce SR Ca^{2+} release events involving Ca^{2+} release via inositol 1,4,5-trisphosphate ($InsP_3$) receptors ($InsP_3Rs$). How the relatively modest Ca^{2+} release via $InsP_3Rs$ elicits this action is not resolved. Here we investigated whether the actions of $InsP_3Rs$ on Ca^{2+} handling during ECC were mediated by a direct influence on dyadic Ca^{2+} levels and whether this mechanism contributes to the effects of ET-1. Using a dyad-targeted genetically encoded Ca^{2+} reporter, we found that $InsP_3R$ activation augmented dyadic Ca^{2+} fluxes during Ca^{2+} transients and increased Ca^{2+} sparks. RyRs were required for these effects. These data provide the first direct demonstration of GPCR/$InsP_3$ effects on dyadic Ca^{2+} and support the notion that Ca^{2+} release via $InsP_3Rs$ influences Ca^{2+} transients during ECC by facilitating the activation and recruitment of proximal RyRs. We propose that this mechanism contributes to neurohormonal modulation of cardiac function.

Introduction

The contraction of cardiomyocytes required for the pumping action of the heart is brought about via excitation-contraction coupling (ECC) (Bers, 2002; Gilbert et al., 2020). Underlying this process, the action potential-mediated opening of voltage-gated L-type Ca^{2+} channels (LTCC) on the sarcolemma evokes a brief Ca^{2+} influx into the cell that is amplified by ryanodine receptors (RyRs) on the sarcoplasmic reticulum (SR). This process of Ca^{2+}-induced Ca^{2+} release (CICR) occurs in cellular microdomains termed dyads that are formed by juxtaposition of LTCCs in the sarcolemma and RyRs in the SR within a narrow 12-15 nm junctional cleft (Sun et al., 1995). In ventricular cardiomyocytes, due to T-tubular invaginations of sarcolemma (TTs), these release sites are distributed across the entire volume of the cardiomyocyte, thereby facilitating a synchronized and cell-wide release of Ca^{2+} from the SR during cell depolarization (Brette and Orchard, 2003).

Through alteration of Ca^{2+} dynamics, circulating and local mediators regulate the strength of cardiomyocyte contraction to meet hemodynamic needs. Although, catecholamines play a pivotal role in this process, other autocrine/paracrine hormones including endothelin-1 (ET-1) and angiotensin II (Ang II) also contribute (Mayourian et al., 2018). Under disease conditions, where their circulating levels are often increased, these mediators contribute to pathology, for example stimulation of pro-arrhythmic activity, including induction of spontaneous Ca^{2+} release events (Hiroe et al., 1991; McMurray et al., 1992; Signore et al., 2013; Stewart et al., 1992; Van De Wal et al., 2006; Yorikane et al., 1993).

Inositol 1,4,5-trisphosphate ($InsP_3$) induced Ca^{2+} release (IICR) via SR-localized $InsP_3$ receptors ($InsP_3R$) contributes to the effects of $G\alpha_q$-associated G protein coupled receptors (GPCR) activation on cardiomyocyte Ca^{2+} handling. GPCR engagement produces an increase in intracellular $InsP_3$ via phospholipase C dependent hydrolysis of phosphatidyl inositol 4,5 bisphosphate (Drawnel et al., 2013). Although expression of $InsP_3R$ (predominantly the type 2 isoform; $InsP_3R2$) in the heart of various mammalian species is well described, the interactions between IICR and ECC are less consistent, particularly in healthy cardiomyocytes, and shows variation between species (Blanch i Salvador and Egger, 2018; Domeier et al., 2008; Harzheim et al., 2010, 2009; Ljubojevic et al., 2014; Proven et al., 2006; Signore et al., 2013; Smyrnias et al., 2018; Wu et al., 2006; Zima and Blatter, 2004). Indeed, while in rabbit, inotropic effects were observed (Domeier et al., 2008), IICR did not contribute to the inotropic action of ET-1 in rat (Harzheim et al., 2009; Smyrnias et al., 2018). Elsewhere, in human and mouse cardiomyocytes,

GPCR/$InsP_3$/$InsP_3$R axis activation augmented pacing-evoked Ca^{2+} transients and cell contraction (Signore et al., 2013). While, these effects of $InsP_3$ on healthy cardiomyocytes may be beneficial, the effects of $InsP_3$R activation are amplified in disease contributing to pathological increases in spontaneous Ca^{2+} release events and to arrhythmogenic Ca^{2+} transients (Blanch i Salvador and Egger, 2018; Harzheim et al., 2009; Nakayama et al., 2010; Proven et al., 2006; Signore et al., 2013). These deleterious aspects of $InsP_3$ signaling arise due to an increase in expression of $InsP_3$R and levels of GPCRs and their ligands that promote generation of $InsP_3$ (Go et al., 1995; Harzheim et al., 2010; Regitz-Zagrosek et al., 1995; Tsutsumi et al., 1998; Zolk et al., 1999).

Despite the lack of consistency in the effects of $InsP_3$ on Ca^{2+} transients between species and studies, a Ca^{2+} mobilizing activity of $InsP_3$ is universally reported (Blanch i Salvador and Egger, 2018; Domeier et al., 2008; Harzheim et al., 2009; Horn et al., 2013). However, these specific actions of $InsP_3$ often require analysis in the absence of the bulk changes in Ca^{2+} associated with ECC, precluding a full understanding of the mechanism by which IICR modulates ECC-associated Ca^{2+} transients. Under these conditions, the actions of $InsP_3$ are manifest as an increase in Ca^{2+} sparks and/or a depletion of the SR Ca^{2+} store (Blanch i Salvador and Egger, 2018; Domeier et al., 2008; Harzheim et al., 2009; Horn et al., 2013; Wullschleger et al., 2017; Zima and Blatter, 2004). Notably, RyRs are in general required for this activity of $InsP_3$ to be fully manifest. Together, these data indicate that $InsP_3$Rs are functionally expressed in cardiomyocytes and that the flux of Ca^{2+} via these receptors is small relative to RyRs. Based on these studies, we and others have proposed that despite their minor capacity to mobilize Ca^{2+} by themselves, through signaling crosstalk with RyRs, $InsP_3$Rs acquire the capacity to influence ECC, including stimulation of pro-arrhythmic activity (Domeier et al., 2008; Harzheim et al., 2009; Wullschleger et al., 2017).

While dyadic co-localization of $InsP_3$Rs and RyRs has been reported, enabling inter channel crosstalk (Harzheim et al., 2009), $InsP_3$Rs have also been suggested to reside on regions of the SR distinct from those occupied by RyRs (Bare et al., 2005; Ljubojevic et al., 2014; Mohler et al., 2005). Although both scenarios could allow for $InsP_3$R-RyR signaling crosstalk, by generating a greater increase in Ca^{2+} local to the RyR, co-localization of $InsP_3$Rs with RyRs in the dyad would be significantly more effective in promoting channel crosstalk. This could occur either through a direct activation via CICR or by bringing RyRs closer to threshold for activation by Ca^{2+} arising from voltage-gated Ca^{2+} channels and/or from Ca^{2+} arising from neighboring

RyRs. Functional evidence supporting a role for IICR in modulation of dyadic RyR and Ca^{2+} dynamics is however lacking.

In this study, we therefore tested the hypothesis that IICR elicits its effects on Ca^{2+} transients through elevating dyadic Ca^{2+}, thereby either facilitating recruitment of RyRs or by enhancing Ca^{2+} fluxes via RyR clusters. To address these questions, we deployed a recently described dyad-targeted genetically encoded Ca^{2+} reporter GCaMP6f-triadin (targeted to the dyad by fusion with triadin) (Shang et al., 2014). In contrast to techniques employing inorganic dyes, this reporter allows the direct measurement of Ca^{2+} dynamics during ECC in intact cardiomyocytes at individual dyads. Indeed, while linescan imaging of Ca^{2+} transients can provide insights into regional regulation of Ca^{2+} release, including by hormonal agonists, a heavy cytosolic buffering to restrict Ca^{2+} signal to the site of generation is required to shed light on the activity of individual dyads (Song et al., 1998). Although used for analysis of dyadic Ca^{2+} dynamics during ECC, the capacity for GCaMP6f-triadin to detect hormonally-induced changes in Ca^{2+} release kinetics in the dyad has not however previously been tested.

Here, we demonstrated the utility of GCaMP6f-triadin to detect the changes in dyadic Ca^{2+} fluxes expected by catecholamines and then took advantage of this property to assess the effect of stimulation with ET-1 and $InsP_3$ on dyadic Ca^{2+} signals in rat ventricular cardiomyocytes. Using live cell imaging of dyadic Ca^{2+} transients, we showed that ET-1 increased spatial recruitment and Ca^{2+} flux at individual release sites, independently of SR Ca^{2+} load. Importantly, augmented dyadic Ca^{2+} release was attenuated by $InsP_3R$ inhibition. Furthermore, we demonstrated increased frequency of Ca^{2+} sparks in response to ET-1, using the dyadic reporter, indicating their localization to this domain. Together, our results suggest that IICR signals to RyRs in the dyad, thereby increasing the likelihood of their activation and SR Ca^{2+} release. We propose that through this mechanism, ET-1 elicits its effects to increase the fidelity of release site activation and to augment dyadic SR Ca^{2+} release fluxes.

Results

GCaMP6f-triadin reports Ca^{2+} changes at individual dyads during the Ca^{2+} transient

Appropriate targeting of GCaMP6f-triadin to the dyad in rat ventricular cardiomyocytes was first assessed by confocal imaging. Analysis of deconvolved confocal images revealed a striated distribution of GCaMP6f-triadin throughout the cardiomyocyte volume (Fig. 1i). By examination of GCaMP6f-triadin distribution in cardiomyocytes immunostained with

antibodies against the type 2 RyR and sarcolemmal/TTs proteins (NCX/Cav3), the reporter was found to be mainly associated with RyRs that co-locate with TTs (junctional RyRs) (Fig. 1ii). The degree of co-localization of GCaMP6f-triadin with RyRs is exhibited by the substantial overlap of the fluorescence signal of the two fluorescence channels observed in the images (Fig. 1ii) and quantitated by Mander's co-localization analysis which showed overlap of 90±1.2% of GCaMP6f-triadin with RyRs and 73±4.4% of RyR with GCaMP6f. By distance analysis, 70% of GCaMP6f-triadin was found to be located within 0.2 µm of the nearest RyR cluster center (Fig. 1iii). In addition to proximity to RyRs, ~56% of the GCaMP6f-triadin fluorescence was within 0.2 µm of the skeletonized TTs (Fig. 1iv) (c.f. to 48% of RyR). In agreement with the distance-based analysis, Mander's co-localization analysis of the two labels showed a 64±1.6% overlap of GCaMP6f-triadin with TTs. Together, the overlap of the majority of GCaMP6f-triadin with TTs and RyRs is consistent with its appropriate targeting to dyadic junctions.

Fluorescence responses of GCaMP6f-triadin were next compared with those of non-targeted GCaMP6f, according to the experimental protocol outlined in Fig. 2A. Consistent with reporting of dyadic Ca^{2+} changes during ECC, GCaMP6f-triadin displayed rapid increases in fluorescence at punctate sites across the cell that tracked electrical pacing (Fig. 2Bi). In comparison with the fluorescence changes of non-targeted GCaMP6f during the Ca^{2+} transient, cell-averaged fluorescence changes of GCaMP6f-triadin exhibited a more rapid rate of rise and were 2-fold greater in amplitude (Fig. 2Ci-ii). Given that GCaMP6f-triadin Ca^{2+} affinity is not substantially affected by fusion to triadin (Shang et al., 2014), these data are consistent with greater proximity of GCaMP6f-triadin to dyadic release sites with higher Ca^{2+} concentration than the non-targeted GCaMP6f.

GCaMP6f-triadin fluorescence changes at individual dyads during Ca^{2+} release were next analyzed. The maximal first derivative of the fluorescence increase of the reporter during the upstroke of the Ca^{2+} transient was used as a measure of Ca^{2+} release flux (the maximal rate of Ca^{2+} release). Since this measure preceded substantial contraction, it was not affected by cardiomyocyte contraction and dyad movement. As a measure of synchronicity or temporal dispersion of Ca^{2+} release between dyads, the mean and standard deviation of the latencies of Ca^{2+} release between individual sites and the first Ca^{2+} release site detected in a cell were used. These analyses revealed a substantial temporal dispersion in release site activation and in maximal Ca^{2+} release flux between dyads (Fig. 2Bii and S2A, B). To further probe the advantage of the dyad targeting for measurements of Ca^{2+} responses, responses of non-targeted GCaMP6f

at dyadic regions demarcated using the membrane stain Di-8-ANEPPS were also analyzed. While heterogeneity of release site activation was detected using GCaMP6f, it was substantially lower than for GCaMP6f-triadin (Fig. S2A). Ca^{2+} flux measured with GCaMP6f was also significantly lower and showed less variation between release sites than that measured using GCaMP6f-triadin (Fig. S2B).

To explore the potential for using GCaMP6f-triadin to detect changes in dyadic Ca^{2+} dynamics, its ability to detect alterations in dyadic Ca^{2+} flux during ECC in response to robust stimulation with β-adrenergic agonist (Isoproterenol; Iso) was first investigated. Cell-averaged measurements of GCaMP6f-triadin showed increases in Ca^{2+} flux and Ca^{2+} amplitude of the Ca^{2+} transients following Iso stimulation (Fig. 2Ci-ii). Effects of Iso stimulation were also detected using the non-targeted GCaMP6f but were substantially smaller (Fig. 2Ci-ii). Ca^{2+} dynamics at individual dyads during Iso stimulation was next investigated. Using GCaMP6f-triadin, significant increases in the sensitivity of SR Ca^{2+} release onset, synchrony of release site activation, maximal dyadic Ca^{2+} release flux and the number of active sites were detected in response to Iso (Fig. 2Di-iv). The magnitude of the Iso effects were significantly smaller when reported with the non-targeted GCaMP6f at Di-8-ANNEPS-labeled sites and no inter-site heterogeneity in activation was detected (Fig. 2Di-ii).

Together, these data highlight the requirement of proximity of the reporter to the dyadic nanodomain to gain insight into Ca^{2+} release kinetics, free from contamination by indicator mobility, Ca^{2+} diffusion and cytosolic Ca^{2+} buffering. These data further indicate that GCaMP6f-triadin is a reliable tool to analyze the spatial and temporal synchrony of Ca^{2+} release between dyads and their modulation by hormonal agonists.

The activity and number of dyadic Ca^{2+} release sites during electrically-evoked Ca^{2+} transients are increased by ET-1 independent of SR Ca^{2+} load

Whether alterations in dyadic Ca^{2+} dynamics contribute to the actions of ET-1 on ECC-associated Ca^{2+} transients was next determined according to the protocol indicated (Fig. 3A). Spatially averaged cell-wide measurements of dyad-targeted (Fig. 3B, 3Ci-ii) and non-targeted GCaMP6f (Fig. S3A) both reported significant increases in the rate of rise and amplitude of the whole-cell Ca^{2+} transient, consistent with previous findings using inorganic Ca^{2+} indicators (Harzheim et al., 2009; Proven et al., 2006). As previously described (Proven et al., 2006; Zima and Blatter, 2004), not all cells responded to ET-1 with an alteration in Ca^{2+} transient properties.

Specifically, increases in Ca^{2+} transient amplitude and maximal Ca^{2+} release flux were detected in 11/17 and 15/18 cardiomyocytes using the dyad targeted (Fig. 3Ci-ii) and non-targeted reporters (Fig. S3Aii-iii). In the absence of ET-1, no changes in kinetics or amplitude of the Ca^{2+} transient were detected with either the dyad-targeted or non-targeted reporter (Fig. S3A, B).

The enhanced dyadic Ca^{2+} release kinetics in the ET-1 responding cell population could result from enhanced synchronization of Ca^{2+} release between sites, increased recruitment of release sites and/or increased maximal Ca^{2+} release flux at individual sites. To test between these possibilities, we analyzed GCaMP6f-triadin responses at individual dyads before and after ET-1 stimulation. Analysis of the mean and SD of the latency of Ca^{2+} release revealed no significant effect of ET-1 on Ca^{2+} release site synchrony (Fig. 3Ciii-iv). As indicated by the greater number of lines of high GCaMP6f-triadin fluorescence intensity on the xt plot, (Fig. 3Bi), ET-1 exposure for 10 min induced a significant increase in the number of active Ca^{2+} release sites (Fig. 3Cv). No changes in these parameters were observed in control cardiomyocytes perfused with buffer alone for 10 min (Fig. S3C).

Consistent with its enhancement of SR Ca^{2+} release, ET-1 application also increased maximal Ca^{2+} release flux at individual dyads (Fig. 3Di). After ET-1 application the variability in maximal Ca^{2+} release flux between dyads was however significantly increased, as shown in the frequency distribution of maximal Ca^{2+} release flux at individual release sites (Fig. 3Dii). Whether the greater heterogeneity of max Ca^{2+} release flux following ET-1 application arose due to alteration in the properties of individual release sites or as a result of recruitment of more sites with heterogeneous properties was next investigated. To this end, the effect of ET-1 on the variability of Ca^{2+} release between sites (inter-site) during a Ca^{2+} transient and at individual release sites (intra-site) during consecutive beats was determined. Under control conditions, a substantial variation in maximal Ca^{2+} release flux at individual dyads and between successive beats was observed. Intra-site variability during consecutive Ca^{2+} transients was however greater than inter-site variability during a single Ca^{2+} transient (Fig. 3Fi-iii). While ET-1 stimulation did not affect the inter-site variability in the maximal Ca^{2+} release flux (illustrated by the coefficient of variance (CV)) between different Ca^{2+} release sites (Fig. 3Fii), it significantly reduced the variability in maximal Ca^{2+} release flux at individual dyads between Ca^{2+} transients (Fig. 3Fiii).

Whether an increase in SR Ca^{2+} load contributed to the augmentation of dyadic Ca^{2+} release by ET-1 was next tested. To this end, the effect of ET-1 on the maximal dyadic Ca^{2+}

release flux induced by caffeine, which induces opening of all RyRs independent of sarcolemmal depolarization was next examined. By exhausting the SR Ca^{2+} store, this approach informs on SR Ca^{2+} load and location of SR Ca^{2+} release sites, including those that are not directly coupled to sarcolemmal depolarization. Consistent with its expected mode of action, rapid local application of 20 mM caffeine increased the fluorescence intensity at all dyads demarcated by expression of the targeted Ca^{2+} biosensor, indicating activation of these release sites and release of available Ca^{2+} from the intracellular store (Fig. S3Di-ii). The maximal SR Ca^{2+} release flux following caffeine application was on average 2-fold greater than during electrical pacing (Fig. S3Diii). ET-1 stimulation did not significantly alter the peak of caffeine-induced Ca^{2+} release (Fig. 3E), consistent with an effect of ET-1 on dyadic Ca^{2+} independent of an increase in the SR releasable Ca^{2+}.

Together, these data highlight the plasticity of individual dyads and support the notion that ET-1 augments SR Ca^{2+} release via a mechanism involving recruitment of normally "silent" release sites and by enhancing Ca^{2+} flux at them, suggesting that more RyRs and/or RyR clusters were activated synchronously among/within release sites.

$InsP_3R$ activation underlies increased recruitment of Ca^{2+} release sites by ET-1

The contribution of $InsP_3Rs$ to the enhancement of dyadic Ca^{2+} release by ET-1 was next determined. Our previous studies show the presence of populations of $InsP_3Rs$ that are proximal to RyRs (Harzheim et al., 2009), but their location relative to the dyad and RyRs within the dyad was not determined. Confocal imaging of $InsP_3Rs$ and RyRs in cardiomyocytes immunolabelled with antibodies that recognize the type 2 isoforms of these receptors revealed an overlap of 49.9±1.6% of the two channel types as well as a proportion of $InsP_3Rs$ located between RyR clusters, albeit along the same Z-line (Fig. 4Ai). Consistent with this observation, similar findings regarding to the relative distributions of these channels were obtained using a distance-based analysis (Fig. 4Aii). The location of $InsP_3Rs$ relative to TTs, was next analyzed by confocal imaging of $InsP_3Rs$ labelled using the same anti-type 2 $InsP_3R$ antibody used in Fig 4Ai and TTs immunolabelled using an NCX/Cav3 antibody cocktail. By this analysis, 32±0.7% of $InsP_3Rs$ were found to overlap with TTs (Fig. 4Aiii). In line with these data, distance-based analysis of $InsP_3R$/TT localization revealed ~30% of $InsP_3Rs$ to be located <0.2 μm from TTs (Fig. 4Aiv). This observation suggests that via close localization, Ca^{2+} signals through $InsP_3R$ could influence Ca^{2+} release via RyRs clusters. In line with the overlap of $InsP_3Rs$ and RyRs with the

TTs, immunofluorescent labeling revealed significant co-localization of GCaMP6f-triadin with the $InsP_3R2$ (Fig. 4Ai-ii).

The influence of $InsP_3Rs$ on dyadic Ca^{2+} was examined. To this end, IICR was either stimulated by ET-1 application or suppressed by co-application of the $InsP_3R$ inhibitor 2-aminoethoxydiphenyl borate (2-APB) according to the protocol indicated (Fig. 4B). 2-APB was used at a relatively low concentration of 2 µM previously shown to inhibit $InsP_3Rs$ without effects on pacing induced Ca^{2+} transients in cardiomyocytes (Peppiatt et al., 2003). Consistent with the hypothesis that dyadic Ca^{2+} dynamics were influenced by ET-1 stimulated IICR, 2-APB abrogated the increased maximal Ca^{2+} release flux integrated across all dyadic sites during the Ca^{2+} transient elicited by its application (Fig. 4C, Di). In control experiments, no effects of 2-APB on these parameters were detected (Fig. S4A, B).

The consequence of $InsP_3R$ inhibition on maximal Ca^{2+} release flux and its heterogeneity at individual Ca^{2+} release sites in cardiomyocytes exposed to ET-1 was next assessed. To allow direct comparison between conditions, measurements at 10 min after treatment were normalized to those before. ET-1 application increased the maximal Ca^{2+} release flux at individual dyads, which was inhibited by 2-APB (Fig. 4Dii). 2-APB application also reduced the number of active release sites during ECC in ET-1 stimulated cells (Fig. 4Diii). Application of 2-APB alone did not affect dyadic maximal Ca^{2+} release flux (Fig. S4C-F). Similarly, 2-APB application did not show any effect on SR releasable Ca^{2+}, as determined by caffeine-induced SR Ca^{2+} release (Fig. 4Div). Together, these data indicate that Ca^{2+} release via $InsP_3Rs$ in the vicinity of dyadic RyRs mediates the increase in maximal Ca^{2+} flux and sensitivity of local dyadic SR Ca^{2+} release as well as the spatial recruitment of active release sites observed in ET-1 stimulated cardiomyocytes.

ET-1 stimulation induced more frequent and larger Ca^{2+} sparks in quiescent ventricular cardiomyocytes

To further examine $InsP_3R$-RyR interactions in dyadic Ca^{2+} release, elementary Ca^{2+} release events were analyzed. As Ca^{2+} sparks are the building blocks of the Ca^{2+} transient generated via the coordinated activation of RyRs, their analysis provides information regarding how activation of $InsP_3Rs$ influence the overall Ca^{2+} release process. In these experiments, as the Ca^{2+} reporter is dyadic, Ca^{2+} release events are highly localized with dyadic RyR clusters and have been termed nanosparks (Shang et al., 2014).

297 Ca^{2+} nanosparks were recorded in quiescent intact ventricular cardiomyocytes,
298 following 10 min pacing, in the presence of buffer or ET-1 (according to the protocol in Fig. 5Ai).
299 Representative recordings of Ca^{2+} nanosparks are shown in the xt images and F/F_0 traces in
300 figure 5Aii and iii. As shown in the xt images, Ca^{2+} nanosparks were reported at dyadic sites of
301 GCaMP6f-triadin localization. As would be expected following conditioning with low pacing
302 frequency, Ca^{2+} nanosparks were relatively rare under control conditions (observed in 11/16
303 cardiomyocytes) (Fig. 5Aii, Bi). The frequency of these events was however significantly
304 increased following ET-1 application (15/16 cardiomyocytes displayed Ca^{2+} release events) (Fig.
305 5Aiii, Bi). The spatiotemporal properties of the Ca^{2+} nanosparks were not affected by ET-1, while
306 their associated maximal Ca^{2+} release flux was significantly larger (Fig. 5Bii-vi). Although, the
307 means of the amplitudes and FWHM of Ca^{2+} nanosparks were unaffected by ET-1, a significant
308 increase in the variance of these measures was observed ($p=0.0001$ and $p<0.0001$ for amplitude
309 and FWHM respectively). The distribution of FWHM was also broader than in control, revealing
310 a subpopulation of smaller Ca^{2+} release events (Fig. 5Biii). Interestingly, a population of Ca^{2+}
311 nanosparks with FWHM ranging between 0.99 and 1.6 μm (those typically observed under
312 control conditions) were of larger amplitude in ET-1 treated cells (Fig. 5C), suggesting an
313 increased recruitment of RyRs. To uncover whether the limited changes in Ca^{2+} nanospark
314 parameters observed in ET-1 stimulated cells impacted dyadic Ca^{2+} signaling, their signal mass
315 ($1.206 \times \Delta F/F_0 \times FWHM^3$) (Chandler et al., 2003), which reflects the quantum of Ca^{2+}
316 released with each event, and spark-mediated Ca^{2+} leak (product of mass and frequency) were
317 calculated. ET-1 treatment did not however significantly alter Ca^{2+} nanospark mass or associated
318 leak (Fig. 5D).
319 The requirement for RyRs for the action of ET-1 was next investigated. Tetracaine
320 inhibition of RyRs resulted in an almost complete inhibition of Ca^{2+} nanosparks in control cells
321 as well as in cells exposed to ET-1 (Fig. 5Bi). In the few remaining Ca^{2+} release events detected
322 under control and ET-1 stimulated conditions, RyR inhibition also resulted in significant
323 decreases in the amplitude, size (FWHM), duration (FDHM) and rise time (TTP). Maximal Ca^{2+}
324 release flux of these events was not affected however (Fig. 5Bii-vi). As the analysis of Ca^{2+}
325 release event properties in RyR inhibited cells is based on very few events in a few cells, effects
326 of ET-1 cannot be ruled out.
327 Together, these data support the notion that ET-1 augments dyadic Ca^{2+} nanospark
328 frequency via stimulation of Ca^{2+} release through $InsP_3Rs$ and its activation of RyRs.

Direct $InsP_3R$ activation evoked more frequent and heterogeneous Ca^{2+} nanosparks

To probe the functional interaction between $InsP_3Rs$ and RyR and its regulation of dyadic Ca^{2+} signaling independent of other cellular consequences of ET-1 stimulation, Ca^{2+} release via $InsP_3Rs$ was directly induced by $InsP_3$ liberated from a caged precursor (cag-$InsP_3$) (Fig. 6A). Uncaging of $InsP_3$ resulted in an increase in Ca^{2+} nanospark frequency in individual cells when compared to controls (Fig. 6Bi). No effect of $InsP_3$ uncaging on the amplitude, duration (FDHM), rise time (TTP) and maximal Ca^{2+} release flux of nanosparks was detected, while their size (FWHM) was decreased (Fig. 6Bii-vi). $InsP_3$ uncaging did however induce an increase in the variance in amplitude ($p=0.0106$) and FWHM ($p<0.0001$) of the Ca^{2+} nanosparks (Fig. 6Bii-iii). No effect of $InsP_3$ uncaging on Ca^{2+} nanospark mass and Ca^{2+} leak was detected (Fig. 6Bvii-viii). The above results suggest that IICR increases the probability of Ca^{2+} nanospark generation at dyadic sites by both recruiting RyR clusters and more RyRs within a cluster.

The effects of direct stimulation of $InsP_3Rs$ on dyadic Ca^{2+} in the absence of RyRs activation were next examined. To this end, Ca^{2+} release events were recorded with RyR inhibition according to the protocol outlined in Fig 6C. Application of tetracaine alone led to an almost complete cessation of Ca^{2+} release events. The few remaining events had a lower FWHM than those detected in control cells (Fig. 6D and Table 1). Due to the low number of observed events and their great variability, we could not reliably conclude whether these Ca^{2+} release events arose from incompletely inhibited RyRs or through the opening of $InsP_3R$ clusters (Table 1). However, $InsP_3$ uncaging under conditions of RyR inhibition with tetracaine produced a gradual but significant increase in the fluorescence of the dyadic reporter that was not detected in control cardiomyocytes in which $InsP_3$ was not uncaged (Fig. 6E). This increase in fluorescence is shown as a small increase in fluorescence at dyadic sites (brighter regions) in the xt plots of raw fluorescence, and more clearly, in the profiles of fluorescence intensity normalized to pre photo-stimulation levels and the histograms of averaged data.

Discussion

Here we tested the hypothesis that signaling crosstalk between dyadic $InsP_3Rs$ and RyRs contributed to the actions of ET-1 on Ca^{2+} transients during ECC in ventricular cardiomyocytes. Our investigation was enabled through the use of a dyad targeted GFP-based Ca^{2+} indicator, which allowed analysis of dyadic Ca^{2+} with high temporal and spatial resolution. The data generated provides for the first time an analysis of modulation of dyadic Ca^{2+} by neurohormonal

agents and their signaling via $InsP_3Rs$ in intact cardiomyocytes. Applying this approach, we showed that ET-1 treatment recruits Ca^{2+} release sites and augments maximal Ca^{2+} release flux during ECC without modulating SR Ca^{2+} load. Furthermore, we demonstrated that activation of dyadic $InsP_3Rs$ is necessary for the action of ET-1 on kinetics of local Ca^{2+} signals. Moreover, we show that Ca^{2+} release via RyRs is required for the effect of IICR to be manifest.

Application of GCaMP6f-triadin to study dyadic Ca^{2+} signals

While electrophysiological and modelling approaches have provided quantitative insights into dyadic Ca^{2+} changes on a cell wide level, analysis of Ca^{2+} release during ECC, particularly at individual dyads has been challenging (Acsai et al., 2011; Cannell et al., 2013). Contributing to the inaccessibility of dyadic Ca^{2+} dynamics to analysis by inorganic Ca^{2+} indicator dyes is dye diffusion and rapid dissipation of dyadic Ca^{2+} changes (Sipido and Wier, 1991; Song et al., 1998). To deal with these issues, Ca^{2+} changes have been measured at individual dyads through the use of a high-affinity Ca^{2+} dye in the presence of strong but slow buffer to restrict Ca^{2+} diffusion in the cytosol (Song et al., 1998). This technique is however disruptive to ECC and requires low frequency electrical stimulation (~ 0.1 Hz) to allow SR Ca^{2+} loading and buffer equilibration. Fundamental aspects of Ca^{2+} release can also be uncovered through analysis of Ca^{2+} sparks although this is generally performed in the absence of electrical pacing. Genetically engineered Ca^{2+} probes targeted to the dyadic cleft (Despa et al., 2014; Shang et al., 2014) have enabled measurements of Ca^{2+} dynamics at individual dyads in intact cardiomyocytes under physiological conditions and thus provided new insights into their activity during ECC. As we show here, dyad movement during cardiomyocyte contraction makes tracking of individual dyads for the full duration of a Ca^{2+} transient difficult, precluding accurate measurement of transient amplitude. The onset of Ca^{2+} release and maximal Ca^{2+} release flux, which provide important information regarding the sensitivity and magnitude of Ca^{2+} flux central to our study, occurred prior to the onset of substantial contraction and could thus be used without interference. This allowed us to avoid pharmacological inhibitors of contraction and their associated issues (Gwathmey et al., 1991; Kolega, 2004). Analysis of these parameters showed significant variability in the activation time of Ca^{2+} release and maximal Ca^{2+} release flux at individual dyads during ECC. These data likely reflect the reported differences in RyR density and distribution per cluster, the number of clusters per dyad, and location relative to TTs membrane (Dries et al., 2013; Galice et al., 2018; Kolstad et al., 2018). The rapid equalization of

391 Ca^{2+} across the contiguous SR store makes it unlikely that the heterogeneity of SR Ca^{2+} release
392 is due to inhomogeneous SR Ca^{2+} loading (Picht et al., 2011). Consistent with this notion,
393 heterogeneity of Ca^{2+} release between dyads was significantly reduced when caffeine was used
394 to activate RyRs.

395 Using GCaMP6f-triadin, we report the first description of an enhancement and spatial
396 synchronization of SR Ca^{2+} release specifically in the dyad during ECC in response to stimulation
397 with the β-agonist isoproterenol. While recruitment and augmentation of dyadic Ca^{2+} release
398 has been previously reported using inorganic dyes, these analyses were not based on
399 measurements at individual dyads during ECC. Rather, these data came from regional analysis
400 of Ca^{2+} release or were from Ca^{2+} spikes at low pacing frequency. Our new data and analysis
401 therefore directly demonstrate the potential for using this reporter for analysis of changes in
402 dyadic SR Ca^{2+} release in response to hormonal or pharmacological interventions. Thus,
403 although Ca^{2+} binding properties of the reporter were considered not ideal for detection of the
404 large and rapid changes in Ca^{2+} at the dyad, the detection of increase in spatiotemporal
405 synchrony of SR Ca^{2+} release, augmented maximal Ca^{2+} release flux and recruitment of
406 previously inactive dyads by β-agonists would however indicate capacity of the reporter to
407 sense these changes. Further, increases in SR Ca^{2+} flux and number of active release sites were
408 also detected after caffeine application, which rapidly and synchronously activates SR Ca^{2+}
409 release, thus reducing variability due to desynchronized activation by Ca^{2+} entry across the
410 sarcolemma. Considering the relatively high dissociation constant of GCaMP6f-triadin (K_d=632
411 nM), yet lower than of synthetic dyes, and that Ca^{2+} reaches 10-100 µM in the dyad during CICR
412 (Acsai et al., 2011; Shannon et al., 2004), rapid saturation of the reporter was expected. The
413 relatively slow "turn-on" kinetics (k_{on} ~ 20 ms) of GCaMP6f (Chen et al., 2013; Helassa et al.,
414 2016), which likely does not allow equilibration to the steady state at saturating but short
415 transient Ca^{2+} increases, is suggested to allow it to report the Ca^{2+} changes occurring in the
416 dyad.

417 Dyadic localization of the indicator was also sufficient to detect β-adrenergic mediated
418 enhancement of Ca^{2+} release during ECC in cell-wide analysis of linescan imaging experiments.
419 Despite measurement of fluorescent changes at TT demarcated with a membrane dye, effects
420 of β-adrenergic agonist were less apparent when a non-targeted GCaMP6f was employed.
421 Specifically, in contrast to the more heterogeneous rise in local TTs-jSR Ca^{2+} release reported by
422 the dyad-targeted GCaMP6f, Ca^{2+} signals among dyads across the cell (highlighted by

membrane stain) were homogenous when measured by the non-targeted reporter. This difference is however likely explained by Ca^{2+} diffusion and the homogenous distribution of the non-targeted reporter. In particular, after release, Ca^{2+} rapidly diffuses from its source where it is detected by the homogenously distributed reporter. As our measure of latency represents the time difference between the release site studied and the first Ca^{2+} release detected, the lower latencies of the non-targeted reporter reflect the homogenization of detection of Ca^{2+} release when using such a reporter. Together, these data highlight the substantial advantages of using a dyad targeted reporter to measure the influence of hormonal mediators on SR Ca^{2+} release and moreover to dissect out mechanisms of regulation of individual Ca^{2+} release sites in this process.

$InsP_3$-induced Ca^{2+} release raises dyadic Ca^{2+} facilitating RyR activation

While IICR modulates Ca^{2+} transients during ECC following GPCR engagement, the mechanism by which the relatively small Ca^{2+} flux via $InsP_3Rs$ influences the bulk changes in Ca^{2+} mediated by RyRs during ECC is not fully determined. Indeed, the low conductance of $InsP_3Rs$ (~3 fold lower than RyRs) (Foskett et al., 2007; Zima and Blatter, 2004) together with a substantially lower expression level than RyRs would suggest little capacity to impact global Ca^{2+}. Consistently, $InsP_3R$ activation in cells in which RyRs are inhibited leads to the generation of either a low frequency of Ca^{2+} puffs or 'silent' events (Harzheim et al., 2009; Horn et al., 2013; Wullschleger et al., 2017; Zima and Blatter, 2004).

Remarkably, by using the dyadic targeted GCaMP6f to analyze Ca^{2+} release at individual dyads during the Ca^{2+} transient, we uncovered that ET-1 acted to both recruit more dyads and to augment Ca^{2+} flux at individual dyads during the Ca^{2+} transient. ET-1 did not influence dyadic Ca^{2+} dynamics in every cardiomyocyte however and the magnitude of change varied substantially among the cells. This high degree of variability was previously suggested to result from variation between cardiomyocytes in the expression and/or ratio of ET_A and ET_B receptors (Domeier et al., 2008; Proven et al., 2006; Zima and Blatter, 2004). In addition to enhanced spatial recruitment of dyads during the Ca^{2+} transient, ET-1 also reduced the variability in dyadic Ca^{2+} release between Ca^{2+} transients. These observations could be explained by increased cooperativity of RyRs/RyR clusters activity within the single release site and/or increased Ca^{2+} sensitivity of RyRs (Galice et al., 2018).

453 The capacity for ET-1 to influence dyadic Ca^{2+} was dependent on Ca^{2+} release via $InsP_3Rs$.
454 The localization of $InsP_3Rs$ to dyadic sites, as reported here and previously, supports this activity
455 of $InsP_3Rs$. As shown previously for effects on global Ca^{2+} transients and Ca^{2+} sparks, the
456 augmentation of dyadic Ca^{2+} signaling by IICR downstream of ET-1 was sensitive to $InsP_3R$
457 inhibition with 2-APB. Further, photoliberation of $InsP_3$ from a caged precursor was sufficient
458 to modulate dyadic Ca^{2+}, ruling out the requirement for other downstream effectors of GPCR
459 signaling. Using this approach, the frequency but no other properties of dyadic Ca^{2+} release
460 events was increased, suggesting enhanced recruitment of the machinery underlying Ca^{2+}
461 sparks. In support of this notion, inhibition of RyRs prevented the action of $InsP_3$. These data
462 are in agreement with conclusions drawn in previous studies that did not directly measure
463 dyadic Ca^{2+} release. The data presented here however now demonstrate the important
464 contribution of dyadic $InsP_3R$-RyR channel crosstalk to the mechanism by which $InsP_3Rs$ can
465 influence global Ca^{2+} changes in healthy ventricular cardiomyocytes but have little effect when
466 acting alone. Several studies, including from our lab, have however detected Ca^{2+} release events
467 (Ca^{2+} puffs) in the presence of RyR inhibition in atrial cardiomyocytes and ventricular
468 cardiomyocytes of different animal species (Harzheim et al., 2009; Wullschleger et al., 2017;
469 Zima and Blatter, 2004). $InsP_3R$ expression is however greater in the atrial and diseased
470 ventricular cardiomyocytes in which these observations were made. In the present study, we
471 were unable to directly resolve Ca^{2+} puffs. The amplitude of Ca^{2+} puffs is ~20% of Ca^{2+} sparks
472 (Zima and Blatter, 2004), which approaches the signal-to-noise detection threshold of a
473 confocal microscope. Although, Ca^{2+} puffs may be generated at clusters containing as few as 2
474 $InsP_3Rs$ in mammalian cells, a substantial increase in Ca^{2+} flux and frequency is observed when
475 the number of $InsP_3Rs$ forming a cluster is greater (Dickinson et al., 2012). Considering the low
476 abundance of functionally active $InsP_3R$ in healthy ventricular cardiomyocytes, it is therefore
477 not surprising that Ca^{2+} puffs were only rarely detected in the absence of active RyRs. Rather,
478 consistent with induction of Ca^{2+} release via $InsP_3Rs$, we observed an increase in baseline Ca^{2+}
479 levels when $InsP_3Rs$ were directly activated by $InsP_3$ under conditions of RyR blockade. This
480 eventless release is reminiscent of that previously described using a diffusible Ca^{2+} indicator
481 when cardiomyocytes were stimulated with ET-1 or $InsP_3$ (Blanch i Salvador and Egger, 2018;
482 Horn et al., 2013).

483 The increase in Ca^{2+} nanospark frequency induced by $InsP_3$ uncaging indicates that the
484 numerous other cellular targets of ET-1 including L-type Ca^{2+} channels (He et al., 2000; Lauer et

al., 1992; Watanabe and Endoh, 1999), K^+ channels (James et al., 2001), Na^+/Ca^{2+} exchanger (Yang et al., 1999; Zhang et al., 2006), Na^+/H^+ exchanger (Kramer et al., 1991) are not required for ET-1 modulation of dyadic Ca^{2+}. $InsP_3R$ may however influence cardiomyocyte electrophysiology. Indeed, dyadic localization could allow IICR regulation of the L-type Ca^{2+} current and localization of $InsP_3Rs$ in the neighborhood of the electrogenic Na^+/Ca^{2+} exchanger (NCX; located in microdomains along the TTs that are distinct to release sites), is reported to modulate the electrical properties of ventricular cardiomyocytes that may lead to arrhythmia (Mohler et al., 2005; Signore et al., 2013).

To explain how $InsP_3$ elicited its effects, we reasoned that either Ca^{2+} release via $InsP_3Rs$ served to directly activate RyR clusters or facilitated their activation by Ca^{2+} arising from other sources including via LTCC and RyRs (Cannell et al., 2013; Kolstad et al., 2018; Walker et al., 2015; Wang et al., 2004; Wescott et al., 2016). The normal cytosolic Ca^{2+} sensitivity of cardiac RyRs is inherently low, resulting in infrequent openings at cytosolic Ca^{2+} concentrations <1 µM (Xu et al., 1996). Modelling studies predict that concentrations of upwards of 10 µM are in fact required for RyR activation indicating that gating of RyRs is only achieved when they are in close vicinity of a Ca^{2+} source (Cannell et al., 2013). Ca^{2+} release via proximal $InsP_3Rs$ could therefore act via CICR to stimulate RyR openings. Further, based on the notion that clusters rapidly shut down when RyRs numbers are low or are disorganized, IICR could also act to maintain cluster activity and increase spark fidelity (Walker et al., 2015).

Via inducing a leak of Ca^{2+} from the SR, IICR is reported to lead to a reduction in SR Ca^{2+} load (Blanch i Salvador and Egger, 2018). As lower SR Ca^{2+} results in a reduction in RyR-mediated Ca^{2+} release and spark termination (Györke and Györke, 1998), this depletion of the SR Ca^{2+} store could thus lead to a reduction in Ca^{2+} flux during the Ca^{2+} transient. We did not however see such an effect of ET-1 activation of IICR under the pacing conditions used for recordings of electrically-evoked Ca^{2+} release, suggesting that in healthy cardiomyocytes, homeostatic mechanisms are sufficient to maintain SR Ca^{2+} levels in the face of IICR activation. Further supporting the ability of homeostatic mechanisms to counter substantial Ca^{2+} leak, we also did not see any $InsP_3$ stimulated elevation in diastolic Ca^{2+} levels in paced cardiomyocytes or in quiescent cardiomyocytes in which RyRs were inhibited. These findings are in agreement with our previous study (Smyrnias et al., 2018) and are in line with findings in rabbit cardiomyocytes which showed a substantially lower Ca^{2+} leak via $InsP_3Rs$ than via RyRs (Zima et al., 2010).

Conclusions

Via activation of dyadic $InsP_3R$-dependent Ca^{2+} signaling to RyRs and a consequent increase in the fidelity of Ca^{2+} spark generation, ET-1, and possibly other hormones that act via $G\alpha_q$ coupled GPCRs modulates SR Ca^{2+} release during ECC in ventricular cardiomyocytes (Fig 7). Through this recruitment of dyadic RyRs clusters and sensitization of the Ca^{2+} release process, ET-1 stimulation augments Ca^{2+} transients and/or promotes an increase in potentially arrhythmogenic extra-systolic Ca^{2+} release events. These effects can be especially detrimental under the circumstances of RyRs post-translational modifications such as by CaMKII and ROS that sensitize them to Ca^{2+}.

Materials and methods

Ethical statement. All experimental procedures were approved by the in-house ethical committee (*Ethische Commissie Dierproeven,* KU Leuven), with permit number P070/2018 and comply with European legislation (European Commission Directive 2010/63/EU) on animal care.

Adult rat ventricular cardiomyocyte isolation, culture and adenoviral infection. Cardiomyocytes were enzymatically isolated from male 6-7-week-old Wistar Kyoto rats (weight 180-210 g) purchased from Harlan Laboratories (Horst, The Netherlands). Briefly, rats were deeply anesthetized by I.P. injection of pentobarbital (80 mg/kg) supplemented with heparin (2500 units/kg) in the same syringe to prevent blood coagulation, and subsequently sacrificed by cervical dislocation. The heart was removed from the rat via bilateral thoracotomy, placed on a Langendorff perfusion apparatus and digested with collagenase II (Worthington Biochemical Corp. Lakewood, HJ, USA) at 37°C as previously described (Smyrnias et al., 2018). Culture and viral infections were performed with modifications from that previously described (Drawnel et al., 2012). Freshly isolated cardiomyocytes were plated on 18 mm coverslips coated with 25 µg/ml laminin (Gibco, #23017015) and thereafter cultured in M199 medium (Sigma-Aldrich, #M7528), supplemented with 0.1% BSA, 1% insulin-transferrin-selenium and penicillin/streptomycin, 5 mM creatine, 2 mM L-carnitine, 5 mM taurine. One hour after plating, unattached cells were removed and remaining cardiomyocytes were infected with adenovirus carrying the target gene at a multiplicity of infection of 100. Cardiomyocytes were used for experiments after 48 h in culture. Cardiomyocytes that responded to electrical stimulation and did not show spontaneous activity were selected for analysis (Fig. S1A).

Molecular biology and preparation of adenoviruses. The recombinant adenoviral plasmid that contained GCaMP6f-triadin gene was kindly provided by Prof. Heping Cheng (Peking University, China) (Shang et al., 2014). pGP-CMV-GCaMP6f was a gift from Douglas S. Kim (Addgene plasmid # 40755) (Chen et al., 2013). Adenoviruses were generated using the AdEasy Adenoviral vector system (Agilent Technologies, #240009). Briefly, the coding region of the gene to be expressed was cloned into the pShuttle-CMV vector, after which it was recombined into pAdEasy-1 vector by LR recombinase reaction in *E.coli*. After sequence-verification the adenoviral recombinant plasmid was linearized with *PacI* and after purification with SureClean Plus beads (Bioline, #BIO-37047), was transfected into HEK293 cells. Crude adenovirus was harvested after 10-14 days. This crude viral preparation was used for large-scale amplification of virus in HEK293 cells, which was purified using the Vivapure AdenoPack 100 RT kit (Sartorius, #VS-AVPQ102). Adenoviral stock titer was determined using an end-point dilution assay.

Confocal Ca^{2+} imaging. On the day of experiment, coverslips were mounted in the imaging chamber (Multichannel systems; model #RC-49MFSH), supplemented with perfusion and aspiration system, and a solenoid-controlled local perfusion system was positioned near the cell to allow continuous perfusion and rapid switching between control and agonist/blocker solutions. Throughout the experiment, cells were constantly perfused with normal Tyrode solution (135 mM NaCl, 5.4 mM KCl, 10 mM HEPES, 10 mM D-glucose, 2 mM $MgCl_2$ and 1 mM $CaCl_2$ at pH 7.35). All experiments were performed at room temperature on cardiomyocytes electrically paced with a pair of platinum electrodes at a stimulation frequency of 0.5 Hz. A voltage was set at the value required to evoke contraction in >90% of cardiomyocytes. To visualize TTs, cardiomyocyte membranes were fluorescently labeled with Di-8-ANEPPS (ThermoFisher, #D3167; 5 µM) dye for 5 min. Ca^{2+} imaging was performed using a Nikon A1R confocal microscope through a Nikon Apo 60x Oil λS DIC N2 (1.4 NA) oil immersion objective, the pinhole was set to 1 A.U. achieving a Z-section thickness of 0.42 µm. Ca^{2+} transients were recorded at 512 lines/s with a pixel size of 0.19 – 0.22 µm.

Reagents. Pharmacological agents were from Sigma-Aldrich (Belgium) and concentrations used were as follows: isoproterenol 10 nM (Iso; #I6504), endothelin-1 100 nM (ET-1; #E7764), angiotensin II 1 µM (Ang II; #A9525), 2-aminoethyl diphenylborinate 2 µM (2-APB; #D9754), tetracaine 1 mM (#T7508;) and caffeine 20 mM (#C0750). $InsP_3$ AM 1 µM (cag-$InsP_3$; SiChem GmbH, #cag-iso-2-145-1).

Ca^{2+} release measurements and protocols. Local and spatially averaged SR Ca^{2+} release signals were measured using GCaMP6f-triadin (GCaMP6f-T) and non-targeted GCaMP6f. For analysis of dyadic Ca^{2+} release during Ca^{2+} transients, cardiomyocytes were paced at 0.5 Hz. At the end of experiment, to determine the SR Ca^{2+} load and all recruitable Ca^{2+} release sites, electrical stimulation was stopped and 20 mM caffeine rapidly applied. To measure the effect of treatment on the frequency and properties of elementary Ca^{2+} release events, pacing was paused for 30 s to record spontaneous Ca^{2+} release events. For experiments involving photo-release of $InsP_3$, cardiomyocytes were loaded with cag-$InsP_3$ diluted to 1 µM in Pluronic F-127 (ThermoFisher, #P30000MP) for 1 h. $InsP_3$ was photo-released at user-defined cellular regions using the 405 nm laser integrated in the Nikon A1R confocal imaging system. The laser exposure required to achieve uncaging was determined empirically by imaging Ca^{2+} release in HeLa cells, which express $InsP_3$Rs. 4 exposures of 250 ms duration (pixel dwell time is 7.5 µs) with the laser at 100% was found to achieve optimal uncaging.

Image analysis. Analysis of local, cytosolic Ca^{2+} release and elementary Ca^{2+} release events was performed using Fiji (Schindelin et al., 2012) and Matlab (The MathWorks Inc., Natick, MA). Acquired fluorescent linescan images were processed using custom-written routines in ImageJ. Parameters of Ca^{2+} signals were calculated from the extracted profiles of fluorescence change using Matlab. Amplitude and maximal rate of SR Ca^{2+} release of spatially averaged Ca^{2+} transients were analyzed after normalization to resting fluorescence levels (F/F_0) in Matlab. The time course of fluorescence was averaged for 5 pixels around the center of the identified release site. Synchrony of Ca^{2+} release was assessed as previously described (Song et al., 2001), by measuring the latency of Ca^{2+} release onset in relation to the earliest release site and measuring the standard deviation of these values. The peak of the first derivative of fluorescence change ($max(\Delta F_0/ms)$) during Ca^{2+} release was used as a measure of maximal Ca^{2+} release flux from the SR as previously described (Sipido and Wier, 1991). Only active release sites that displayed a fluorescence change exceeding the threshold of 5 x SD x F_0 were included in the analysis. For each release site, kinetic parameters of Ca^{2+} release were averaged from the seven consecutive Ca^{2+} transients to reduce the effect of beat-to-beat variability of stochastic Ca^{2+} release via RyRs. SR Ca^{2+} content was assessed by rapidly applying 20 mM caffeine and measuring the amplitude of the elicited Ca^{2+} transient.

The SparkMaster plugin implemented in ImageJ was used to analyze Ca^{2+} spark parameters (Picht et al., 2007). The Ca^{2+} spark event detection was set at 6 times the standard deviation of

609 the background noise over the mean value of the background. This value was required to
610 accommodate for the non-homogeneous distribution of targeted GCaMP6f. Detected events
611 were further verified by manual analysis. Parameters analyzed included spark frequency
612 (normalized to cell length and time), amplitude ($\Delta F/F_0$), size (full width at half-maximal
613 amplitude; FWHM), duration (full duration at half-maximal amplitude), rise time (time to peak)
614 and maximal Ca^{2+} release rate (max(ΔF_0/ms)). Ca^{2+} spark mass was calculated according to the
615 formula 1.206 x $\Delta F/F_0$ x $FWHM^3$ (Chandler et al., 2003). Spark-mediated Ca^{2+} leak was calculated
616 as the product of spark mass and frequency.
617 **Immunofluorescence and imaging.** Cardiomyocytes expressing GCaMP6f-triadin were fixed
618 with 1% paraformaldehyde (PFA) in normal Tyrode solution for 5 min at room temperature. The
619 distribution of GCaMP6f-triadin relative to SR Ca^{2+} release channels was investigated by
620 confocal microscopy. In brief, dual labelling was performed using rabbit anti-RyR2 (gift from
621 Prof. V. Sorrentino, University of Sienna; 1:200) (Giannini et al., 1995) or anti-$InsP_3R2$ (Atlas
622 Antibodies, HPA059144; Lot#R82918; 1:100) primary antibodies in combination with a cocktail
623 of mouse anti-NCX1 (Swant, R3F1; Lot#mr05; 1:200) and anti-caveolin-3 (BD Bioscience,
624 N610420; 1:200) primary antibodies designed to stain the sarcolemma/TTs as previously
625 described (Hou et al., 2015; Munro et al., 2016). For simultaneous visualization of $InsP_3Rs$ and
626 RyRs, dual labeling was performed with mouse anti-RyR1 (clone 34C, which also recognizes type
627 2 RyR) (Invitrogen, #MA3-925; Lot#TG268734; 1:200) and rabbit anti-$InsP_3R2$ (Atlas Antibodies,
628 HPA059144; 1:100) primary antibodies. Cardiomyocytes were permeabilized with PBS
629 containing 0.4% Triton X-100 (diluted from Surfact-Amps detergent solution, ThermoFisher,
630 #28314) for 15 min at room temperature, followed by blocking with either 5% normal goat
631 serum (NGS) (Sigma-Aldrich, #S26-M) in PBS (for RyR2 antibody) or Image-iT Signal Enhancer
632 ($InsP_3R$ antibody; ThermoFisher, #I36933) for 1 h at room temperature. Primary antibodies
633 were applied overnight at 4°C in a buffer composed of PBS, 0.1% Triton X-100, 2% BSA and 2%
634 NGS. Appropriate secondary antibodies, conjugated with either Alexa Fluor 568 (goat anti-
635 rabbit, ThermoFisher, # A-11036) or Alexa Fluor 647 (goat anti-mouse, ThermoFisher, # A-
636 21236), were applied at a dilution of 1:100 or 1:500 for goat anti-rabbit and 1:200 for goat anti-
637 mouse to stain $InsP_3R2$, RyR2 and TTs/sarcolemma respectively. All secondary antibodies were
638 incubated for 2 h at room temperature. Cardiomyocytes were mounted on glass slides in
639 Vectashield containing DAPI (Vector Laboratories, #H-1200-10), and images were acquired
640 using a Nikon A1R confocal microscope configured on a Nikon Ti2 equipped with a Nikon Apo

60x/1.4 NA (MRD71600) oil immersion objective. The pinhole was set to achieve a Z-section thickness of 0.45 µm. Images were acquired with voxel size set at 0.11 x 0.11 x 0.2 µm.

Acquired image stacks were deconvolved using Huygens Professional version 19.04 (Scientific Volume Imaging, The Netherlands), using the CMLE algorithm with the signal to noise ratio set at 20 and iterations to 40. A single image of the stack from the cell central plane was used to assess relative expression of proteins. After images for each protein staining were thresholded, the relative distances were measured using a custom-written macro in ImageJ and were calculated as Euclidean distance between the center of two nearest clusters. Additionally, overlap between two proteins of interest was calculated in analogy with Mander's coefficient.

GCaMP6f-triadin expression analysis of confocal images. Quantitative analysis of cellular GCaMP6f-triadin protein expression relative to RyRs and TTs was based on confocal immunofluorescence imaging as described above. To exclude sub-sarcolemmal cellular regions of the analysis, the cell mask was created by blurring the RyR2 images (Gaussian Blur, sigma 25 pixels) and consecutive dilation (25 pixels). Similarly, nuclei and perinuclear regions were removed from GCaMP6f-triadin, TTs and RyR2 images. To create a mask of these regions, DAPI images were consecutively smoothed (Mean, radius 1 pixel), blurred (Gaussian Blur, sigma 15 pixels) and binarized. The immunofluorescence signal pattern of GCaMP6f-triadin, TTs and RyR2 was segmented by Fiji operations. 1) GCaMP6f-traidin images were background subtracted (rolling ball radius: 5 pixels), smoothed (Mean, radius 2 pixels), and global Moments thresholding was used to binarize the GCaMP6f-triadin signals. 2) TT images were smoothed (Median, radius 2 pixels), segmented by local Bernsen thresholding (radius: 15) and consecutively skeletonized. 3) RyR2 images were background subtracted (rolling ball radius: 5 pixels), smoothed (Median, radius 2 pixels) and segmented by local Otsu thresholding (radius: 12). Watershed function was applied to separate adjacent clusters that were segmented together. Binarized images were then used to determine the percentage of GCaMP6f-triadin clusters overlapping with RyR2 signals and TTs. For overlap analysis, we accepted clusters that ranged between partial and mutually complete overlap in binarized images. The skeleton of TTs was used to calculate the Euclidean distance between TTs and GCaMP6f-triadin clusters.

InsP_3R expression analysis of confocal images. Quantitative analysis of cellular expression of InsP_3Rs was performed as described for GCaMP6f-triadin except for image processing and segmentation methods. 1) RyR2 images were background subtracted (rolling ball radius: 10), smoothed (Mean, radius 1 pixel) and segmented by local Bernsen thresholding (radius: 5). 2)

673 $InsP_3R2$ images were background subtracted (rolling ball radius: 15), smoothed (Median, radius
674 1 pixel) and binarized by local Otsu threshold (radius: 15). 3) TT images were smoothed (Median,
675 1 pixel), segmented by local Otsu threshold (radius: 18) and consequently skeletonized.
676 **Statistical analysis.** All individual data points are shown in dot plots, with each dot representing
677 a cell. Normal distribution of data was assessed with D'Agostino & Pearson omnibus normality
678 testing (α=0.05). Data are presented mean ± SEM or before-after measurement along to the
679 calculated effect sizes with 95% confidence interval. Statistical comparisons were made using
680 paired or unpaired Student's t test, Wilcoxon matched-pairs signed rank test (paired data, non-
681 normal distribution), Mann-Whitney U (unpaired data, non-normal distribution) and ordinary
682 one-way ANOVA with Bonferroni *post hoc* test to compare >2 groups. A repeated measures
683 two-way ANOVA test with Bonferroni *post hoc* testing was applied for pharmacological
684 interventions. Difference in distributions of maximal dyadic Ca^{2+} release fluxes and Ca^{2+} sparks
685 parameters was assessed using equal variance (F) test. Statistical analysis was performed using
686 GraphPad Prism 9 software (GraphPad Software, La Jolla California USA) and statistical
687 significance was set at $p<0.05$. The number of animals ($N_{animals}$), cells (n_{cells}), release sites ($n_{release\ sites}$)
688 and Ca^{2+} release events are given in the figure legends. Sample sizes were determined by
689 power analysis based on data in our previous publication on similar parameters (Harzheim et
690 al., 2009). We assessed the presence of outliers by using ROUT method implemented in
691 Graphpad (with Q = 1%).

692 **Acknowledgments**

693 We thank Roxane Menten for assistance with animal handling and cell isolation, Prof. Heping
694 Cheng for the GCaMP6f-triadin construct and Prof. Douglas S. Kim & Genie project (Howard
695 Hughes Medical Institute, USA) for the pGP-CMV-GCaMP6f plasmid. RyR2 antibody was a gift
696 from Prof. Vincenzo Sorrentino (University of Siena, Italy).

697 **Funding Sources**

698 This work was supported by the KU Leuven and the Fund for Scientific Research-Flanders (FWO
699 Project grant [G08861N, Odysseus Project 90663 to H.L.R.]).

700 **References:**

Acsai K, Antoons G, Livshitz L, Rudy Y, Sipido KR. Microdomain [Ca^{2+}] near ryanodine receptors as reported by L-type Ca^{2+} and Na^{+}/Ca^{2+} exchange currents. *J Physiol*. 2011; 589. 10:2569-2583. doi:10.1113/jphysiol.2010.202663

Bare DJ, Kettlun CS, Liang M, Bers DM, Mignery GA. Cardiac type 2 inositol 1,4,5-trisphosphate receptor: Interaction and modulation by calcium/calmodulin-dependent protein kinase II. *J Biol Chem*. 2005; 280(16):15912-15920. doi:10.1074/jbc.M414212200

Bers DM. Cardiac excitation-contraction coupling. *Nature*. 2002; 415(6868):198-205. doi:10.1038/415198a.

Blanch i Salvador J, Egger M. Obstruction of ventricular Ca^{2+}-dependent arrhythmogenicity by inositol 1,4,5-trisphosphate-triggered sarcoplasmic reticulum Ca^{2+} release. *J Physiol*. 2018; 596(18):4323-4340. doi:10.1113/JP276319

Brette F, Orchard C. T-tubule function in mammalian cardiac myocytes. *Circ Res*. 2003; 92(11):1182-1192. doi:10.1161/01.RES.0000074908.17214.FD

Cannell MB, Kong CHT, Imtiaz MS, Laver DR. Control of sarcoplasmic reticulum Ca^{2+} release by stochastic RyR gating within a 3D model of the cardiac dyad and importance of induction decay for CICR termination. *Biophys J*. 2013; 104:2149-2159. doi:10.1016/j.bpj.2013.03.058

Chandler WK, Hollingworth S, Baylor SM. Simulation of calcium sparks in cut skeletal muscle fibers of the frog. *J Gen Physiol*. 2003; 121(4):311–24. doi/10.1085/jgp.200308787

Chen TW, Wardill TJ, Sun Y, Pulver SR, Renninger SL, Baohan A, Schreiter ER, Kerr RA, Orger MB, Jayaraman V, Looger LL, Svoboda K, Kim DS. Ultrasensitive fluorescent proteins for imaging neuronal activity. Nature. 2013; 499:295-300. doi:doi.org/10.1038/nature12354

Despa S, Shui B, Bossuyt J, Lang D, Kotlikoff MI, Bers DM. Junctional Cleft $[Ca^{2+}]_i$ Measurements Using Novel Cleft-Targeted Ca^{2+} Sensors. *Circ Res*. 2014; 115:339-347. doi:10.1161/CIRCRESAHA.115.303582

Dickinson GD, Swaminathan D, Parker I. The probability of triggering calcium puffs is linearly related to the number of inositol trisphosphate receptors in a cluster. *Biophys J*. 2012; 102(8):1826-1836. doi:10.1016/j.bpj.2012.03.029

728 Domeier TL, Zima A V., Maxwell JT, Huke S, Mignery GA, Blatter LA. IP_3 receptor-dependent $Ca2^+$
729 release modulates excitation-contraction coupling in rabbit ventricular myocytes. *Am J Physiol*
730 *– Heart Circ Physiol*. 2008; 294:H596-H604. doi:10.1152/ajpheart.01155.2007

731 Drawnel FM, Wachten D, Molkentin JD, Maillet M, Aronsen JM, Swift F, Sjaastad I, Liu N,
732 Catalucci D, Mikoshiba K, Hisatsune C, Okkenhaug H, Andrews SR, Bootman MD, Roderick HL.
733 Mutual antagonism between IP_3RII and miRNA-133a regulates calcium signals and cardiac
734 hypertrophy. *J Cell Biol*. 2012; 199(5):783-798. doi: 10.1083/jcb.201111095

735 Drawnel FM, Archer CR, Roderick HL. The role of the paracrine/autocrine mediator endothelin-
736 1 in regulation of cardiac contractility and growth. *Br J Pharmacol.* 2013; 168(2):296-317. doi:
737 10.1111/j.1476-5381.2012.02195.x.

738 Dries E, Bito V, Lenaerts I, Antoons G, Sipido KR, Macquaide N. Selective modulation of coupled
739 ryanodine receptors during microdomain activation of calcium/calmodulin-dependent kinase II
740 in the dyadic cleft. *Circ Res*. 2013;113(11):1242-1252. doi:10.1161/CIRCRESAHA.113.301896

741 Foskett JK, White C, Cheung K-H, Mak D-OD. Inositol Trisphosphate Receptor Ca^{2+} release
742 channels. *Physiol Rev*. 2007; 87:593-658. doi:10.1152/physrev.00035.2006.

743 Galice S, Xie Y, Yang Y, Sato D, Bers DM. Size Matters: Ryanodine Receptor Cluster Size Affects
744 Arrhythmogenic Sarcoplasmic Reticulum Calcium Release. *J Am Heart Assoc*. 2018; 7(13).
745 doi:10.1161/JAHA.118.008724

746 Giannini G, Conti A, Mammarella S, Scrobogna M, Sorrentino V. The ryanodine receptor/calcium
747 channel genes are widely and differentially expressed in murine brain and peripheral tissues. *J*
748 *Cell Biol.* 1995; 128(5):893-904. doi.org/10.1083/jcb.128.5.893.

749 Gilbert G, Demydenko K, Dries E, Puerta RD, Xin J, Sipido K, Roderick HL. Calcium signalling in
750 cardiomyocyte function. *Cold Spring Harb Perspect Biol*. 2020; 12(3).
751 doi:10.1101/cshperspect.a035428

752 Go LO, Moschella MC, Watras J, Handa KK, Fyfe BS, Marks AR. Differential regulation of two
753 types of intracellular calcium release channels during end-stage heart failure. *J Clin Invest*. 1995;
754 95:888-894. doi: 10.1172/JCI117739

755 Gwathmey JK, Hajar RJ, Solaro RJ. Contractile deactivation and uncoupling of crossbridges.
756 Effects of 2,3-butanedione monoxime on mammalian myocardium. *Circ Res.* 1991; 69(5):1280-
757 92. doi: 10.1161/01.res.69.5.1280.

758 Györke I, Györke S. Regulation of the cardiac ryanodine receptor channel by luminal Ca^{2+}
759 involves luminal Ca^{2+} sensing sites. *Biophys J*. 1998; 75(6):2801-2810. doi:10.1016/S0006-
760 3495(98)77723-9

761 Harzheim D, Movassagh M, Foo RS-Y, Ritter O, Tashfeen A, Conway SJ, Bootman MD, Roderick
762 HL. Increased $InsP_3Rs$ in the junctional sarcoplasmic reticulum augment Ca^{2+} transients and
763 arrhythmias associated with cardiac hypertrophy. *Proc Natl Acad Sci USA.* 2009; 106(27):11406-
764 11411. doi:10.1073/pnas.0905485106

765 Harzheim D, Talasila A, Movassagh M, Foo RSY, Figg N, Bootman MD, Roderick HL. Elevated
766 $InsP_3R$ expression underlies enhanced calcium fluxes and spontaneous extra-systolic calcium
767 release events in hypertrophic cardiac myocytes. *Channels (Austin).* 2010; 4(1):67-71.
768 doi:10.4161/chan.4.1.11537

769 He JQ, Pi YQ, Walker JW, Kamp TJ. Endothelin-1 and photoreleased diacylglycerol increase L-
770 type Ca^{2+} current by activation of protein kinase C in rat ventricular myocytes. *J Physiol*. 2000;
771 524(3):807-820. doi:10.1111/j.1469-7793.2000.00807.x

772 Helassa N, Podor B, Fine A, Török K. Design and mechanistic insight into ultrafast calcium
773 indicators for monitoring intracellular calcium dynamics. *Sci Rep*. 2016; 6:28276. doi:
774 10.1038/srep38276

775 Hiroe M, Hirata Y, Fujita N, Umezawa S, Ito H, Tsujino M, Koike A, Nogami A, Takamoto T,
776 Marumo F. Plasma endothelin-1 levels in idiopathic dilated cardiomyopathy. *Am J Cardiol*. 1991;
777 68(10):1114-1115. doi:10.1016/0002-9149(91)90511-I

778 Horn T, Ullrich ND, Egger M. "Eventless" $InsP_3$-dependent SR-Ca^{2+} release affecting atrial Ca^{2+}
779 sparks. *J Physiol*. 2013; 591(8):2103-2111. doi:10.1113/jphysiol.2012.247288

780 Hou Y, Jayasinghe I, Crossman DJ, Baddeley D, Soeller C. Nanoscale analysis of ryanodine
781 receptor clusters in dyadic couplings of rat cardiac myocytes. *J Mol Cell Cardiol.* 2015; 80:45-55.
782 doi:10.1016/j.yjmcc.2014.12.013

James AF, Ramsey JE, Reynolds AM, Hendry BM, Shattock MJ. Effects of endothelin-1 on K^+ currents from rat ventricular myocytes. *Biochem Biophys Res Commun*. 2001; 284(4):1048-1055. doi:10.1006/bbrc.2001.5083

Kolega J. Phototoxicity and photoinactivation of blebbistatin in UV and visible light. *Biochem Biophys Res Commun.* 2004; 320(3):1020-5. doi: 10.1016/j.bbrc.2004.06.045.

Kolstad TR, van den Brink J, Macquaide N, Lunde PK, Frisk M, Aronsen JM, Norden ES, Cataliotti A, Sjaastad I, Sejersted OM, Edwards AG, Lines GT, Louch WE. Ryanodine receptor dispersion disrupts Ca 2+ release in failing cardiac myocytes. Elife. 2018; 7:1-24. doi:10.7554/eLife.39427

Kramer BK, Smith TW, Kelly RA. Endothelin and increased contractility in adult rat ventricular myocytes. Role of intracellular alkalosis induced by activation of the protein kinase C-dependent Na^+-H^+ exchanger. *Circ Res*. 1991; 68(1):269-279. doi:10.1161/01.RES.68.1.269

Lauer MR, Gunn MD, Clusin WT. Endothelin activates voltage-dependent Ca^{2+} current by a G protein-dependent mechanism in rabbit cardiac myocytes. *J Physiol*. 1992; 448(1):729-747. doi:10.1113/jphysiol.1992.sp019067

Ljubojevic S, Radulovic S, Leitinger G, Sedej S, Sacherer M, Holzer M, Winkler C, Pritz E, Mittler T, Schmidt A, Sereinigg M, Wakula P, Zissimopoulos S, Bisping E, Post H, Marsche G, Bossuyt J, Bers DM, Kockskämper J, Pieske B. Early remodelling of perinuclear Ca^{2+} stores and nucleoplasmic Ca^{2+} signalling during the development of hypertrophy and heart failure. *Circulation*. 2014; 130(3):244-255. doi:10.1161/CIRCULATIONAHA.114.008927

Mayourian J, Ceholski DK, Gonzalez DM, Cashman TJ, Sahoo S, Hajar RJ, Costa KD. Physiologic, pathologic, and therapeutic paracrine modulation of cardiac excitation-contraction coupling. *Circ Res*. 2018; 122(1):167-183. doi:10.1161/CIRCRESAHA.117.311589

McMurray JJ, Ray SG, Abdullah I, Dargie HJ, Morton JJ. Plasma endothelin in chronic heart failure. *Circulation*. 1992; 85(4):1374-1379. doi:10.1161/01.CIR.85.4.1374

Mohler PJ, Davis JQ, Bennett V. Ankyrin-B Coordinates the Na/K ATPase, Na/Ca Exchanger, and $InsP_3$ Receptor in a Cardiac T-Tubule/SR Microdomain. *PLoS Biol*. 2005; 3(12):e423. doi:10.1371/journal.pbio.0030423

Munro ML, Jayasinghe ID, Wang Q, Quick A, Wang W, Baddeley D, Wehrens XHT, Soeller C. Junctophilin-2 in the nanoscale organisation and functional signalling of ryanodine receptor clusters in cardiomyocytes. *J Cell Sci*. 2016; 129:4388-4398. doi:10.1242/jcs.196873

Nakayama H, Bodi I, Maillet M, DeSantiago J, Domeier TL, Mikoshiba K, Lorenz JN, Blatter LA, Bers DM, Molkentin JD. The IP_3 receptor regulates cardiac hypertrophy in response to select stimuli. *Circ Res*. 2010; 107(5):659-666. doi:10.1161/CIRCRESAHA.110.220038

Peppiatt CM, Collins TJ, Mackenzie L, Conway SJ, Holmes AB, Bootman MD, Berridge MJ, Seo JT, Roderick HL. 2-Aminoethoxydiphenyl borate (2-APB) antagonises inositol 1,4,5-trisphosphate-induced calcium release, inhibits calcium pumps and has a use-dependent and slowly reversible action on store-operated calcium entry channels. *Cell Calcium*. 2003; 34(1):97-108. doi: 10.1016/S0143-4160(03)00026-5

Picht E, Zima A V, Blatter LA, Bers DM. SparkMaster: automated calcium spark analysis with ImageJ. *Am J Physiol Cell Physiol.* 2007; 293:1073-1081. doi:10.1152/ajpcell.00586.2006.-Ca

Picht E, Zima A V., Shannon TR, Duncan AM, Blatter LA, Bers DM. Dynamic calcium movement inside cardiac sarcoplasmic reticulum during release. Circ Res. 2011; 108:847-856. doi: 10.1161/CIRCRESAHA.111.240234.

Proven A, Roderick HL, Conway SJ, Berridge MJ, Horton JK, Capper SJ, Bootman MD Inositol 1,4,5-trisphosphate supports the arrhythmogenic action of endothelin-1 on ventricular cardiac myocytes. *J Cell Sci*. 2006; 119:3363-3375. doi:10.1242/jcs.03073

Regitz-Zagrosek V, Friedel N, Heymann A, Bauer P, Neuß M, Rolfs A, Steffen C, Hildebrandt A, Hetzer R, Fleck E. Regulation, chamber localization, and subtype distribution of angiotensin II receptors in human hearts. *Circulation*. 1995; 91(5):1461-1471.

Schindelin J, Arganda-Carreras I, Frise E, Kaynig V, Longair M, Pietzsch T, Preibisch S, Rueden C, Saalfeld S, Schmid B, Tinevez JY, White DJ, Hartenstein V, Eliceiri K, Tomancak P, Cordona A. Fiji: An open-source platform for biological-image analysis. *Nat Methods*. 2012; 9(7):676-682. doi:10.1038/nmeth.2019

Shang W, Lu F, Sun T, et al. Imaging Ca^{2+} nanosparks in heart with a new targeted biosensor. *Circ Res*. 2014;114(3):412-420. doi:10.1161/CIRCRESAHA.114.302938

838 Shannon TR, Wang F, Puglisi J, Weber C, Bers DM. A mathematical treatment of integrated Ca
839 dynamics within the ventricular myocyte. *Biophys J*. 2004; 87(5):3351-3371.
840 doi:10.1529/biophysj.104.047449

841 Signore S, Sorrentino A, Ferreira-Martins J, Kannappan R, Shafaie M, Del Ben F, Isobe K, Arranto
842 C, Wybieralska E, Webster A, Sanada F, Ogórek B, Zheng H, Liu X, Del Monte F, D'Alessandro
843 DA, Wunimenghe O, Michler RE, Hosoda T, Goichberg P, Leri A, Kajstura J, Piero A, Marcello R.
844 Inositol 1, 4, 5-trisphosphate receptors and human left ventricular myocytes. *Circulation*. 2013;
845 128(12):1286-1297. doi:10.1161/CIRCULATIONAHA.113.002764

846 Sipido KR, Wier WG. Flux of Ca^{2+} across the sarcoplasmic reticulum of guinea-pig cardiac cells
847 during excitation-contraction coupling. *J Physiol*. 1991; 435(1):605-630.

848 Smyrnias I, Goodwin N, Wachten D, Skogestad J, Aronsen JM, Robinson EL, Demydenko K,
849 Segonds-Pichon A, Oxley D, Sadayappan S, Sipido K, Bootman MD, Roderick HL. Contractile
850 responses to endothelin-1 are regulated by PKC phosphorylation of cardiac myosin binding
851 protein-C in rat ventricular myocytes. *J Mol Cell Cardiol*. 2018; 17:1-18.

852 Song L-S, Sham JSK, Stern MD, Lakatta EG, Cheng H. Direct measurement of SR release flux by
853 tracking "Ca^{2+} spikes" in rat cardiac myocytes. *J Physiol*. 1998;512(3):677-691.
854 doi:10.1111/j.1469-7793.1998.677bd.x

855 Song L-S, Wang S-Q, Xiao R-P, Spurgeon H, Lakatta EG, Cheng H. B-Adrenergic Stimulation
856 Synchronizes Intracellular Ca^{2+} Release During Excitation-Contraction Coupling in Cardiac
857 Myocytes. *Circ Res*. 2001; 88:794-801. doi:10.1161/hh0801.090461

858 Stewart DJ, Cernacek P, Costello KB, Rouleau JL. Elevated endothelin-1 in heart failure and loss
859 of normal response to postural change. *Circulation*. 1992; 85(2):510-517.
860 doi:10.1161/01.CIR.85.2.510

861 Sun X-H, Protasi F, Takahashi M, Takeshima H, Ferguson DG, Franzini-Armstrong C. Molecular
862 architecture of membranes involved in excitation-contraction coupling of cardiac muscle. *J Cell*
863 *Biol*. 1995; 129(3):659-671. doi:10.1083/jcb.129.3.659

864 Tsutsumi Y, Matsubara H, Ohkubo N, Mori Y, Nozawa Y, Murasawa S, Kijima K, Maruyama K,
865 Masaki H, Moriguchi Y, Shibasaki Y, Kamihata H, Inada M, Iwasaka T. Angiotensin II type 2

receptor is upregulated in human heart with interstitial fibrosis, and cardiac fibroblasts are the major cell type for its expression. *Circ Res*. 1998; 83(10):1035-1046.

Van De Wal RMA, Plokker HWM, Lok DJA, Boomsma F, van der Horst FAL, van Veldhuisen DJ, van Gilst WH, Voors AA. Determinants of increased angiotensin II levels in severe chronic heart failure patients despite ACE inhibition. *Int J Cardiol*. 2006; 106(3):367-372. doi:10.1016/j.ijcard.2005.02.016

Walker MA, Kohl T, Lehnart SE, Greenstein JL, Lederer WJ, Winslow RL. On the Adjacency Matrix of RyR2 Cluster Structures. *PLoS Comput Biol*. 2015; 11(11). doi:10.1371/journal.pcbi.1004521

Wang SQ, Stern MD, Ríos E, Cheng H. The quantal nature of Ca^{2+} sparks and in situ operation of the ryanodine array cardiac cells. *Proc Natl Acad Sci USA*. 2004; 101(11):3979-3984. doi:10.1073/pnas.0306157101

Watanabe T, Endoh M. Characterization of the endothelin-1-induced regulation of L-type Ca^{2+} current in rabbit ventricular myocytes. *Naunyn Schmiedebergs Arch Pharmacol*. 1999; 360(6):654-664. doi:10.1007/s002109900130

Wescott AP, Jafri MS, Lederer WJ, Williams GSB. Ryanodine receptor sensitivity governs the stability and synchrony of local calcium release during cardiac excitation-contraction coupling. *J Mol Cell Cardiol*. 2016; 92:82-92. doi:10.1016/j.yjmcc.2016.01.024

Wu X, Zhang T, Bossuyt J, Li X, McKinsey TA, Dedman JR, Olson EN, Chen J, Heller Brown J, Bers DM. Local $InsP_3$-dependent perinuclear Ca^{2+} signalling in cardiac myocyte excitation-transcription coupling. *J Clin Invest*. 2006; 116:675-682. doi: 10.1172/JCI27374

Wullschleger M, Blanch J, Egger M. Functional local crosstalk of inositol 1,4 5- trisphosphate receptor- and ryanodine receptor-dependent Ca^{2+} release in atrial cardiomyocytes. *Cardiovasc Res*. 2017; 113:542-552. doi:10.1093/cvr/cvx020

Xu L, Mann G, Meissner G. Regulation of Cardiac Ca^{2+} Release Channel (Ryanodine Receptor) by Ca^{2+}, H^+, Mg^{2+}, and Adenine Nucleotides Under Normal and Simulated Ischemic Conditions. *Circ Res*. 1996; 79(6):1100-1109. doi:10.1161/01.RES.79.6.1100

Yang HT, Sakurai K, Sugawara H, Watanabe T, Norota I, Endoh M. Role of Na^+/Ca^{2+} exchange in endothelin-1-induced increases in Ca^{2+} transient and contractility in rabbit ventricular

myocytes: Pharmacological analysis with KB-R7943. *Br J Pharmacol*. 1999; 126(8):1785-1795. doi:10.1038/sj.bjp.0702454

Yorikane R, Sakai S, Miyauchi T, Sakurai T, Sugishita Y, Goto K. Increased production of endothelin-1 in the hypertrophied rat heart due to pressure overload. *FEBS Lett*. 1993; 332(1-2):31-34. doi:10.1016/0014-5793(93)80476-B

Zhang YH, Hinde AK, James AF, Hancox JC. Modulation of the Na^+/Ca^{2+} Exchanger by Isoprenaline, Adenosine, and Endothelin-1 in Guinea Pig Ventricular Myocytes*. Ann NY Acad Sci.* 2006; 976(1):535-538. doi:10.1111/j.1749-6632.2002.tb04789.x

Zima A V., Blatter LA. Inositol-1,4,5-trisphosphate-dependent Ca^{2+} signalling in cat atrial excitation-contraction coupling and arrhythmias. *J Physiol*. 2004; 555(3):607-615.

Zolk O, Quattek J, Sitzler G, Schrader T, Nickenig G, Schnabel P, Shimada K, Takahashi M, Böhm M. Expression of Endothelin-1, Endothelin-Converting Enzyme, and Endothelin Receptors in Chronic Heart Failure. *Circulation*. 1999; 99(16):2118-2123. doi:10.1161/01.CIR.99.16.2118

Figure legends:

Figure 1. GCaMP6f-triadin is localized to the dyad in cardiomyocytes.

Analysis of GCaMP6f-triadin distribution in rat cardiomyocytes 48 h post infection. i) Mid-plane image of deconvolved confocal Z-stack of cardiomyocyte overexpressing GCaMP6f-triadin (GCaMP6f-T) (green) with TTs and sarcolemma delineated by NCX/Cav3 labelling in magenta and RyR labelling in grey. ii) 10X magnified view of the section demarcated by the white square in i. Top are deconvolved confocal images and bottom are masks of the deconvolved images showing the distribution of each protein alone and in overlay. iii) Percentage of GCaMP6f-triadin puncta as a function of the Euclidean distance from the center of the nearest RyR cluster. iv) Distribution of distances between centers of NCX/Cav3 and GCaMP6f-triadin puncta. Left of the dashed line are bars indicating distances between centroids that are considered to co-localize. n= 34 cells, N=5 animals.

Figure 2. Dyad targeting of GCaMP6f is required to detect synchronization of Ca^{2+} release during ECC in ventricular cardiomyocytes following β-adrenergic stimulation.

(A) Protocol used for assessment of kinetics and synchrony of dyadic Ca^{2+} release during ECC ± Iso. (**B**) Assessment of dyadic Ca^{2+} signals with non-targeted GCaMP6f and GCaMP6f-triadin. i)

Representative linescan images of fluorescence changes of non-targeted GCaMP6f (left) and GCaMP6-triadin (right) after treatment with Iso. ii) Magnified view of the linescan region depicted by dashed line in i. Right of the respective linescan images are the corresponding profiles of the fluorescence changes detected at junctional release sites from the indicated regions. For non-targeted GCaMP6f, fluorescence is plotted from TT regions labelled with di-8-ANEPPS. (C) Modulatory effect of Iso on Ca^{2+} release during ECC reported by GCaMP6f-triadin and non-targeted GCaMP6f. i) Measurement of Ca^{2+} transient upstroke rate (max(ΔF_0/ms)) under Iso stimulation by GCaMP6f-triadin (left) and non-targeted GCaMP6f (right). ii) Quantification of peak ($\Delta F/F_0$) of cell-wide averaged fluorescence changes recorded using GCaMP6f-triadin (left) and non-targeted GCaMP6f (right) before and after 4 min of Iso stimulation. (D) Ca^{2+} signals properties assessed by GCaMP6f-triadin (GCaMP6f-T) and non-targeted GCaMP6f following Iso stimulation. The latency (i) and synchrony (ii) of Ca^{2+} release, maximal Ca^{2+} release flux at single release sites (iii) and fraction of active dyads (iv) were determined. Data is presented as repeated measures before and after stimulation with the mean difference between the two groups and the 95% confidence interval of this mean. Each data point corresponds to the average value of a parameter from a single cell. Each measurement is the average of 7 consecutive transients. Mean data are from $n_{cells}/N_{animals}$=23/5 for GCaMP6f-triadin and $n_{cells}/N_{animals}$=21/6 for non-targeted GCaMP6f. The number of release sites at baseline and after Iso application is 689/894 and 339/328 for GCaMP6f-triadin and non-targeted GCaMP6f respectively. A paired t test was used for statistical comparison of data.

Figure 3. ET-1 stimulation increases Ca^{2+} release sites recruitment and their rate of Ca^{2+} release in electrically paced ventricular cardiomyocytes.

(A) Protocol used for evaluation of ET-1 effects on dyadic SR Ca^{2+} release during ECC. (B) Linescan recordings of electrically-stimulated cell-wide changes in GCaMP6f-triadin fluorescence before and after 10 min of ET-1. Representative fluorescence images (i) and corresponding normalized fluorescence traces (ii) are presented. (C) Quantification of spatiotemporal synchronicity of release site activation. (i) Peak and (ii) maximal Ca^{2+} release (max(ΔF_0/ms)) of cell-wide Ca^{2+} transients; (iii) latency of Ca^{2+} release onset; (iv) mean deviation of latency of Ca^{2+} release; (v) the percentage of active release sites normalized to the maximal number of potential release sites determined by caffeine application. (D) Effects of ET-1 on SR Ca^{2+} release kinetics. (i) Mean max(ΔF_0/ms) flux ± ET-1; (ii) Distribution of max(ΔF_0/ms) at single

954 release sites before and after stimulation with ET-1. (E) Peak caffeine-induced Ca^{2+} release ± ET-
955 1 treatment. (F) Max(ΔF_0/ms) variance between dyads and at the same dyad between
956 consecutive beats. (i) Superimposition of 7 consecutive Ca^{2+} transients recorded from 3
957 different scanned release sites at baseline. The thick blue line indicates the average
958 fluorescence change at a single release site. (ii) Quantitation of the spatial variability of
959 max(ΔF_0/ms) between single release sites before and after application of ET-1. (iii)
960 Quantification of max(ΔF_0/ms) variability between beats at individual dyad before and after ET-
961 1. The effect of treatment was examined by paired t test. SR Ca^{2+} content was compared by an
962 unpaired t-test. The differences in distributions of max(ΔF_0/ms) at individual release sites was
963 determined with equal variance (f) test. Except for the panels Ci-ii (data from $n_{cells}/N_{animals}$:
964 17/4), mean data are from $n_{cells}/N_{animals}$=11/4 and $n_{cells}/N_{animals}$=18/5 for the ET-1 treated and
965 control groups respectively. n of release sites at baseline and 10 min post-stimulation with ET-
966 1 is 624/669.

967 **Figure 4. Ca^{2+} release via $InsP_3Rs$ is required for the modulation of dyadic Ca^{2+} signals by ET-**
968 **1.**

969 (A) Confocal immunofluorescence analysis of $InsP_3R$ distribution relative to RyRs, TTs (were
970 visualized by co-staining for NCX1 and Cav3) and GCaMP6f-triadin in cardiomyocytes. (i)
971 Magnified view showing relationship between GCaMP6f-triadin (green), $InsP_3Rs$ clusters
972 (magenta) and RyRs clusters (grey). (ii) Magnified view showing the spatial relationship between
973 GCaMP6f-triadin (green), $InsP_3Rs$ clusters (magenta) and TTs (cyan). (iii) Histogram of distances
974 between $InsP_3R$ and their nearest RyRs clusters. The dashed line indicates the threshold
975 distance between cluster centers below which clusters are considered to co-localize. Data are
976 from n_{cells}=21 and $N_{animals}$=3. (iv) Histogram of distances between $InsP_3R$ and nearest TTs. Data
977 are from n_{cells}=22 and $N_{animals}$=3. (B) Protocol for probing the contribution of IICR to the
978 modulation of dyadic SR Ca^{2+} by ET-1. (C) Linescans of Ca^{2+} transients under the different
979 conditions are shown. (D) Analysis of effects of ET-1 ± 2-APB on dyadic Ca^{2+} dynamics. (i)
980 max(ΔF_0/ms) of the Ca^{2+} transient. (ii) The relative change in dyadic max(ΔF_0/ms), (iii) in
981 percentage of active release sites normalized to baseline and (iv) magnitude of caffeine-induced
982 SR Ca^{2+} release are shown. Data are given as repeated measures with each dot representing a
983 single cell in panel Di and as mean ± SEM in panels Dii to iv. Groups were compared by two-way
984 repeated measures ANOVA with Bonferroni post hoc testing (panel D-i), one-way ANOVA test

(panel D-ii to iv). Data are from n_{cells}=16, 14, 12 and 18, $N_{animals}$=4 for control, 2-APB, ET-1 and ET-1 + 2-APB respectively.

Figure 5. ET-1 stimulation induces more frequent and heterogeneous Ca^{2+} nanosparks in quiescent rat ventricular cardiomyocytes.

(A) Measurement of Ca^{2+} nanosparks with GCaMP6f-triadin. (i) Experimental protocol used for analysis Ca^{2+} nanosparks upon stimulation with ET-1. (ii) Confocal linescans under control conditions and (iii) after treatment with 100 nM ET-1. Local changes in (F/F_0) from the release sites indicated by the grey lines are on the left of the images. (B) Effects of ET-1±tetracaine on Ca^{2+} nanospark frequency and spatiotemporal properties of Ca^{2+} nanosparks. (i) Frequency of Ca^{2+} nanosparks, (ii) amplitude, (iii) size, (iv) duration, (v) rise time and (vi) maximal Ca^{2+} release flux. (C) Scatter plot of Ca^{2+} nanospark amplitude in relation to size under control (i) and following ET-1 treatment (ii). (D) Quantification of Ca^{2+} nanospark mass (i) and Ca^{2+} leak (ii) under control and treatment with ET-1. Data in Bi and Dii is presented as mean ± SEM, in Bii-vi and Di as Tukey boxplots with median values under control conditions and following stimulation with ET-1±tetracaine. Groups in Bi were compared with Brown-Forsythe and Welch ANOVA test. Differences in the Ca^{2+} nanospark properties (panels Bii-vi) were compared with Kruskal-Wallis test. Difference between means in Di and Dii were assessed with Mann-Whitney and unpaired t test respectively. Data are from n_{cells}=16, 16 and 31, $N_{animals}$=6, n_{events}=54 (11 cells), 142 (15 cells) and 16 (9 cells) for control, ET-1 and ET-1+tetracaine treated group respectively.

Figure 6. Photo-release of $InsP_3$ evokes more frequent dyadic Ca^{2+} release events/nanosparks

(A) Protocol used to assess frequency and properties of dyadic Ca^{2+} release events following photo-release of $InsP_3$. (B) Frequency and properties of Ca^{2+} release events following photo-release of $InsP_3$. (i) Average data of the effects of $InsP_3$ on Ca^{2+} release event incidence and (ii-vii) Tukey boxplots with median values for amplitude (ii), FWHM (iii), FDHM (iv), time to peak (v), maximal Ca^{2+} release flux (vi) and mass (vii) of Ca^{2+} release events. (viii) Average data of nanospark-mediated Ca^{2+} leak. Data are from n_{cells}=32 and 33, $N_{animals}$=4, n_{events}=156 (23 cells) and 323 (31 cells) for control and $InsP_3$ treated group respectively. (C) Protocol used for the analysis of dyadic SR Ca^{2+} following $InsP_3$ uncaging ± RyR blockade with tetracaine. (D) Representative linescan xt images (i) and fluorescence traces (ii) of rare Ca^{2+} release events after RyR inhibition. (E) In the presence of tetracaine, $InsP_3$ uncaging induces an increase in GCaMP6f-triadin fluorescence. (i) Linescan images of GCaMP6f-triadin fluorescence in cardiomyocytes

loaded ± caged-$InsP_3$ after photo-stimulation. (ii) F/F_0 traces show a gradual increase in fluorescence after $InsP_3$ uncaging in the presence of tetracaine. Values are normalized to the first 100 ms after the 405 nm flash. (iii) The change in fluorescence ($\Delta F/F_0$) between a 1 s average of the signal immediately after uncaging and at the end of 30 s imaging period is shown. Cells with Ca^{2+} release events during this period were excluded from the analysis (4 and 3 cells for control and cells loaded with cag-$InsP_3$). Data is presented as mean ± SEM. n_{cells}=13 and 16, $N_{animals}$=4. Unpaired t-test.

Figure 7. Illustration of the mechanism by which ET-1 via activation of $InsP_3R$ signaling at the dyad modulates SR Ca^{2+} release during ECC.

Following ET-1 stimulation, IICR raises dyadic Ca^{2+} levels, which in turn recruits RyRs during ECC. Through this action, the fidelity of Ca^{2+} spark generation and Ca^{2+} release flux through co-located RyR clusters are increased at single release sites contributing concomitantly to ET-1 modulation of SR Ca^{2+} release during ECC.

Table 1. Comparison of Ca^{2+} release events/nanosparks induced by $InsP_3$ in the presence of tetracaine

	Frequency of Ca^{2+} release events (sparks*100µm^{-1}*s^{-1})	$\Delta F/F_0$	FWHM, µm	FDHM, ms	TTP, ms	max(ΔF_0/ms)	n_{events}/ n_{cells} (Total # of examined cells
Tetracaine	0.15±0.04	0.94±0.27	0.63±0.08	165±148	145±162	49±15	7/4 (13)
Tetracaine + IP_3	0.52±0.78	0.98±0.35	0.99±0.32**	139±50	102±76	74±28*	22/3 (17)

Data are presented as mean ± SD. Spatiotemporal characteristics analyzed include amplitude ($\Delta F/F_0$), FWHM (full width at half maximum), FDHM (full duration at half maximum), TTP (time to peak) and maximal Ca^{2+} release flux (max(ΔF_0/ms)). Unpaired students t-test. * - $p<0.05$, ** - $p<0.01$.

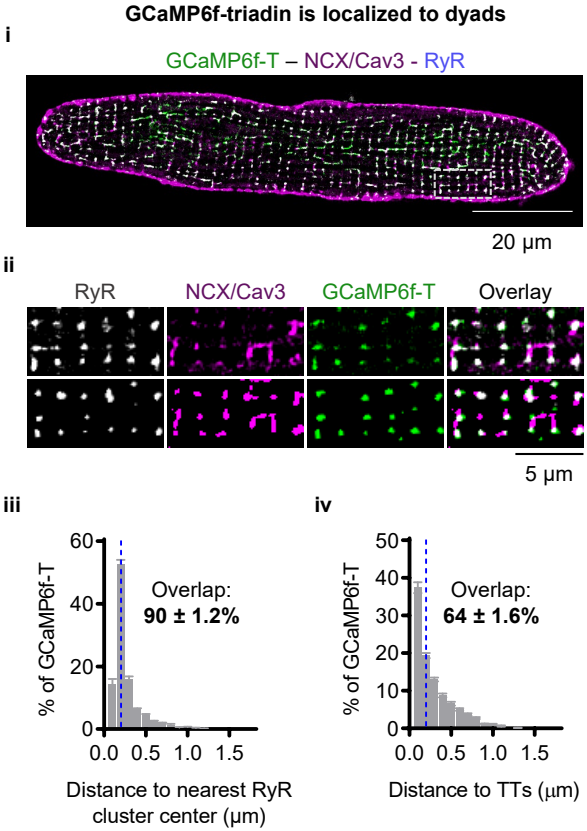
GCaMP6f-triadin is localized to dyads
i
GCaMP6f-T – NCX/Cav3 - RyR
20 µm
ii
RyR
NCX/Cav3
GCaMP6f-T
Overlay
5 µm
iii
% of GCaMP6f-T
Overlap:
90 ± 1.2%
Distance to nearest RyR cluster center (µm)
iv
% of GCaMP6f-T
Overlap:
64 ± 1.6%
Distance to TTs (µm)

Figure 1

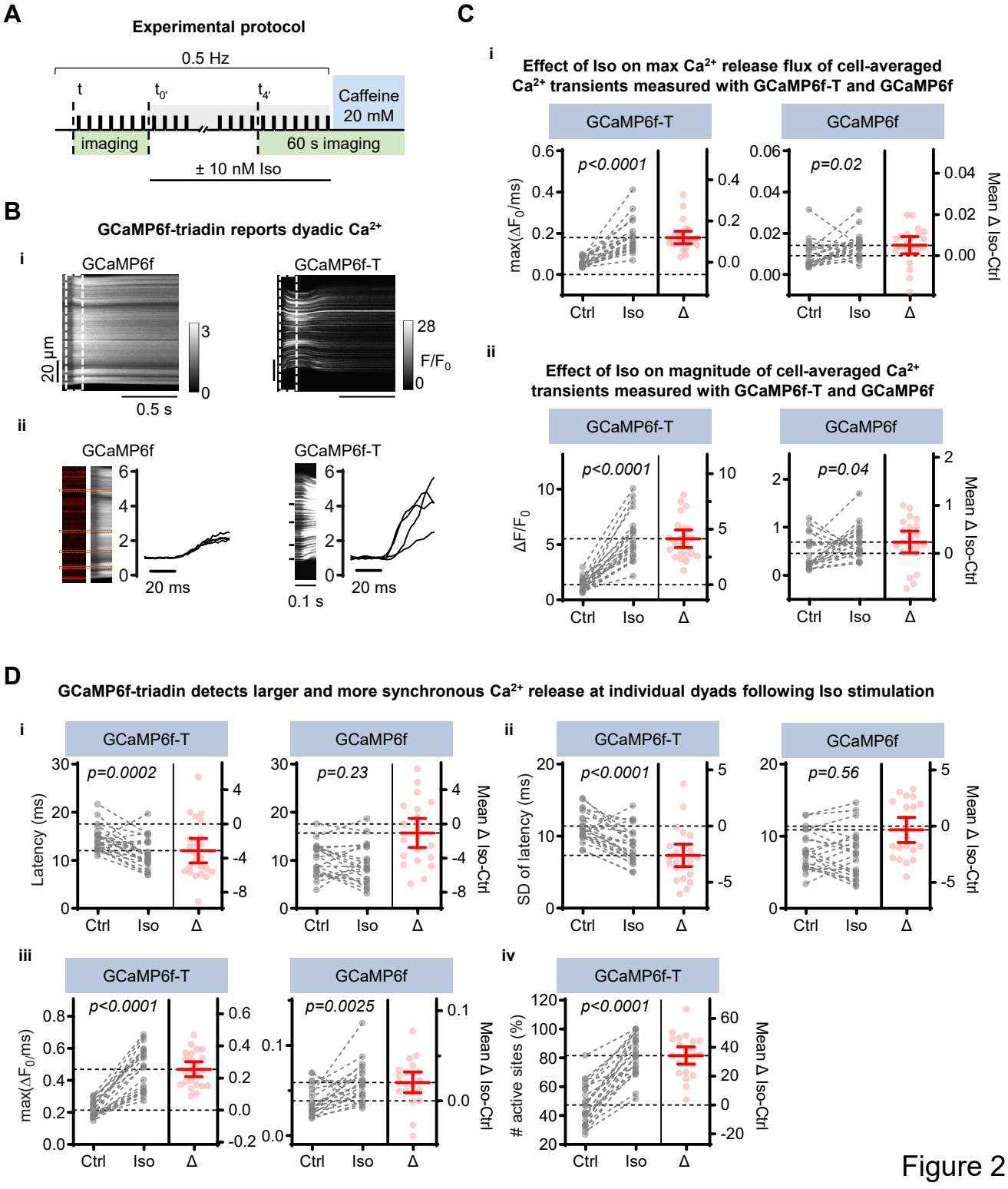
A
Experimental protocol
0.5 Hz
t
t0'
t4'
Caffeine
20 mM
imaging
60 s imaging
± 10 nM Iso
B
GCaMP6f-triadin reports dyadic Ca2+
i
GCaMP6f
GCaMP6f-T
20 µm
0.5 s
3
0
28
F/F0
ii
GCaMP6f
GCaMP6f-T
20 ms
0.1 s
C
i
Effect of Iso on max Ca2+ release flux of cell-averaged Ca2+ transients measured with GCaMP6f-T and GCaMP6f
GCaMP6f-T
GCaMP6f
p<0.0001
p=0.02
max(ΔF0/ms)
Mean Δ Iso-Ctrl
Ctrl
Iso
Δ
ii
Effect of Iso on magnitude of cell-averaged Ca2+ transients measured with GCaMP6f-T and GCaMP6f
GCaMP6f-T
GCaMP6f
p<0.0001
p=0.04
ΔF/F0
Mean Δ Iso-Ctrl
Ctrl
Iso
Δ
D
GCaMP6f-triadin detects larger and more synchronous Ca2+ release at individual dyads following Iso stimulation
i
GCaMP6f-T
GCaMP6f
p=0.0002
p=0.23
Latency (ms)
Mean Δ Iso-Ctrl
Ctrl
Iso
Δ
ii
GCaMP6f-T
GCaMP6f
p<0.0001
p=0.56
SD of latency (ms)
Mean Δ Iso-Ctrl
Ctrl
Iso
Δ
iii
GCaMP6f-T
GCaMP6f
p<0.0001
p=0.0025
max(ΔF0/ms)
Mean Δ Iso-Ctrl
Ctrl
Iso
Δ
iv
GCaMP6f-T
p<0.0001
active sites (%)
Mean Δ Iso-Ctrl
Ctrl
Iso
Δ

Figure 2

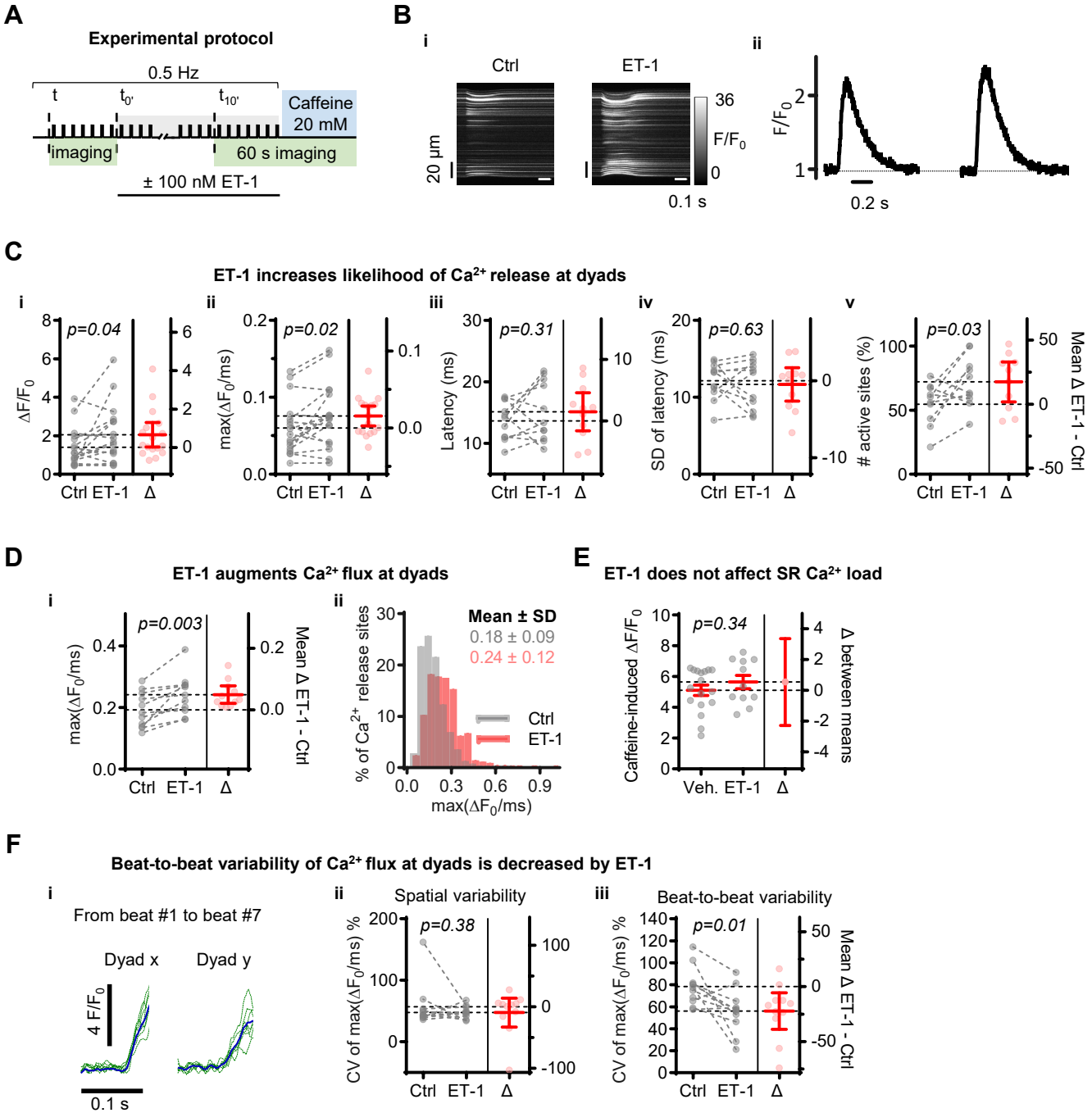
A
Experimental protocol
0.5 Hz
t
t0'
t10'
Caffeine 20 mM
imaging
60 s imaging
± 100 nM ET-1
B
i
Ctrl
ET-1
20 µm
36
F/F0
0
0.1 s
ii
F/F0
2
1
0.2 s
C
ET-1 increases likelihood of Ca2+ release at dyads
i
p=0.04
ΔF/F0
Ctrl ET-1 Δ
ii
p=0.02
max(ΔF0/ms)
iii
p=0.31
Latency (ms)
iv
p=0.63
SD of latency (ms)
v
p=0.03
# active sites (%)
Mean Δ ET-1 - Ctrl
D
ET-1 augments Ca2+ flux at dyads
i
p=0.003
max(ΔF0/ms)
Mean Δ ET-1 - Ctrl
ii
Mean ± SD
0.18 ± 0.09
0.24 ± 0.12
Ctrl
ET-1
% of Ca2+ release sites
max(ΔF0/ms)
E
ET-1 does not affect SR Ca2+ load
p=0.34
Caffeine-induced ΔF/F0
Veh. ET-1 Δ
Δ between means
F
Beat-to-beat variability of Ca2+ flux at dyads is decreased by ET-1
i
From beat #1 to beat #7
Dyad x
Dyad y
4 F/F0
0.1 s
ii
Spatial variability
p=0.38
CV of max(ΔF0/ms) %
iii
Beat-to-beat variability
p=0.01
Mean Δ ET-1 - Ctrl

Figure 3

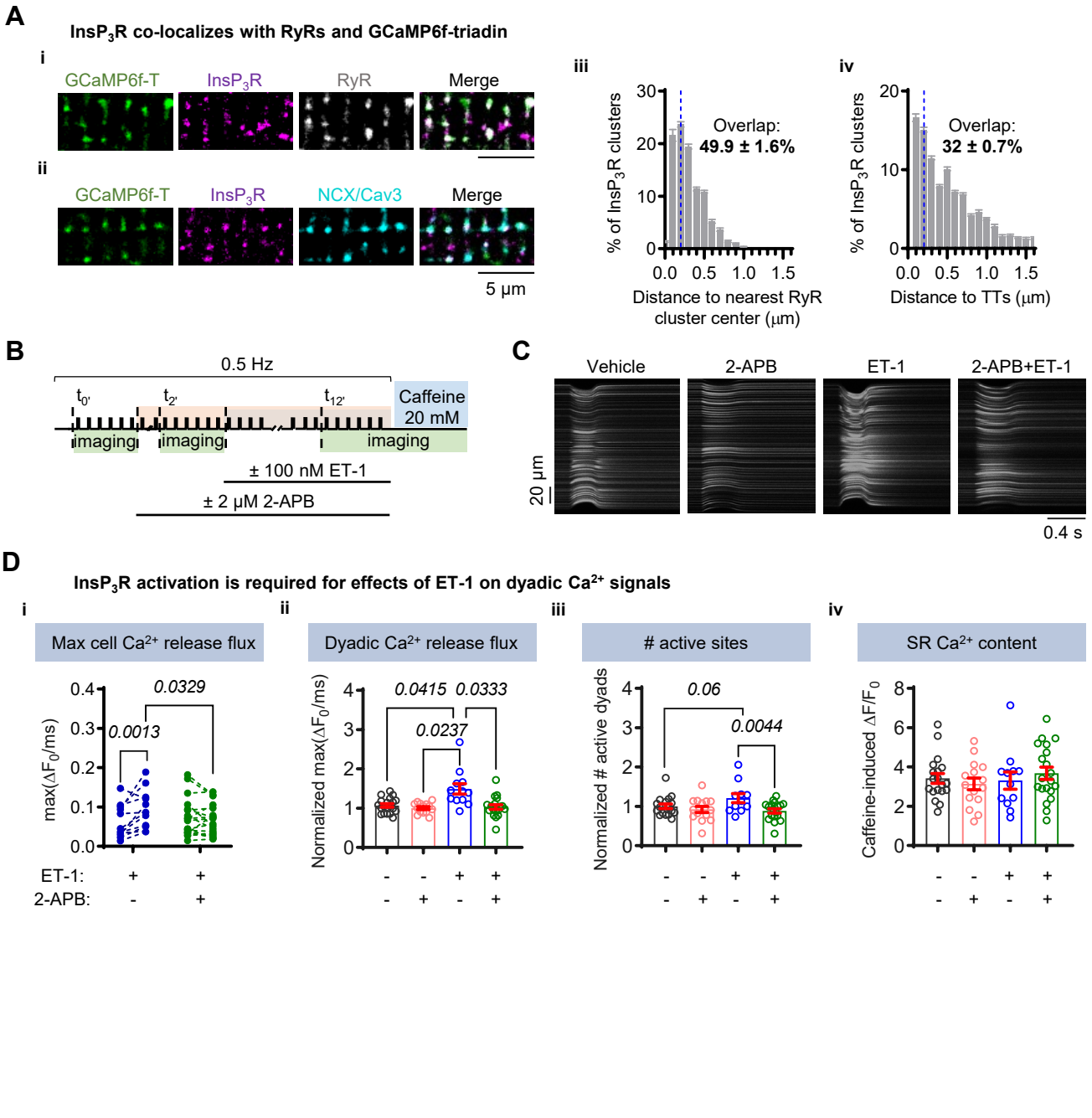
A
InsP3R co-localizes with RyRs and GCaMP6f-triadin
i
GCaMP6f-T
InsP3R
RyR
Merge
ii
GCaMP6f-T
InsP3R
NCX/Cav3
Merge
5 µm
iii
% of InsP3R clusters
Overlap:
49.9 ± 1.6%
Distance to nearest RyR cluster center (µm)
iv
% of InsP3R clusters
Overlap:
32 ± 0.7%
Distance to TTs (µm)
B
0.5 Hz
t0'
t2'
t12'
Caffeine 20 mM
imaging
imaging
imaging
± 100 nM ET-1
± 2 µM 2-APB
C
Vehicle
2-APB
ET-1
2-APB+ET-1
20 µm
0.4 s
D
InsP3R activation is required for effects of ET-1 on dyadic Ca2+ signals
i
Max cell Ca2+ release flux
max(ΔF0/ms)
0.0013
0.0329
ET-1:
2-APB:
ii
Dyadic Ca2+ release flux
Normalized max(ΔF0/ms)
0.0415
0.0333
0.0237
iii
active sites
Normalized # active dyads
0.06
0.0044
iv
SR Ca2+ content
Caffeine-induced ΔF/F0

Figure 4

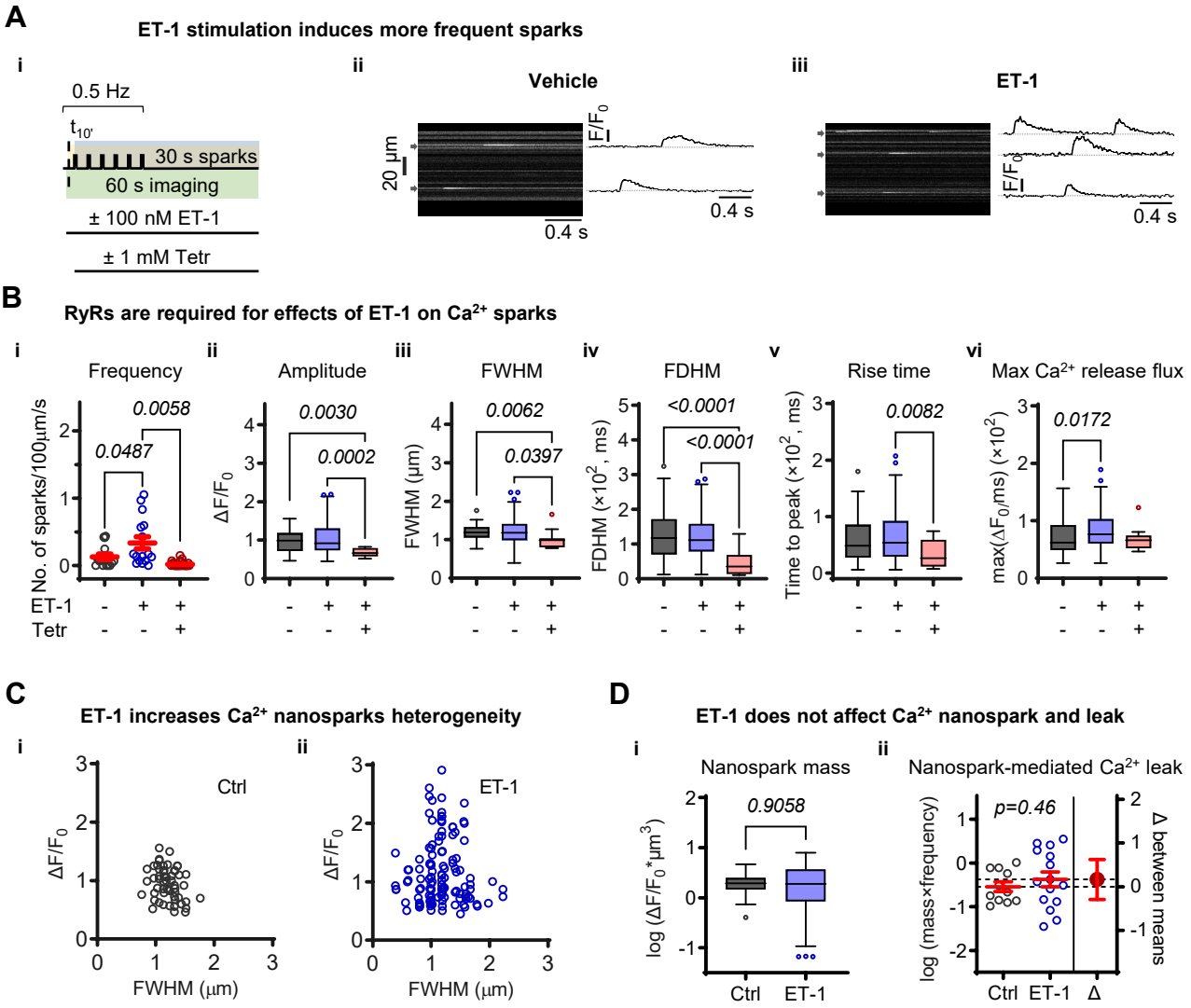
A
ET-1 stimulation induces more frequent sparks
i
0.5 Hz
t10'
30 s sparks
60 s imaging
± 100 nM ET-1
± 1 mM Tetr
ii
Vehicle
20 µm
F/F0
0.4 s
iii
ET-1
F/F0
0.4 s
B
RyRs are required for effects of ET-1 on Ca2+ sparks
i
Frequency
No. of sparks/100µm/s
0.0058
0.0487
ii
Amplitude
ΔF/F0
0.0030
0.0002
iii
FWHM
FWHM (µm)
0.0062
0.0397
iv
FDHM
FDHM (×10², ms)
<0.0001
<0.0001
v
Rise time
Time to peak (×10², ms)
0.0082
vi
Max Ca2+ release flux
max(ΔF0/ms) (×10²)
0.0172
ET-1 - + +
Tetr - - +
C
ET-1 increases Ca2+ nanosparks heterogeneity
i
Ctrl
ΔF/F0
FWHM (µm)
ii
ET-1
ΔF/F0
FWHM (µm)
D
ET-1 does not affect Ca2+ nanospark and leak
i
Nanospark mass
log (ΔF/F0 *µm3)
0.9058
Ctrl ET-1
ii
Nanospark-mediated Ca2+ leak
log (mass×frequency)
p=0.46
Δ between means
Ctrl ET-1 Δ

Figure 5

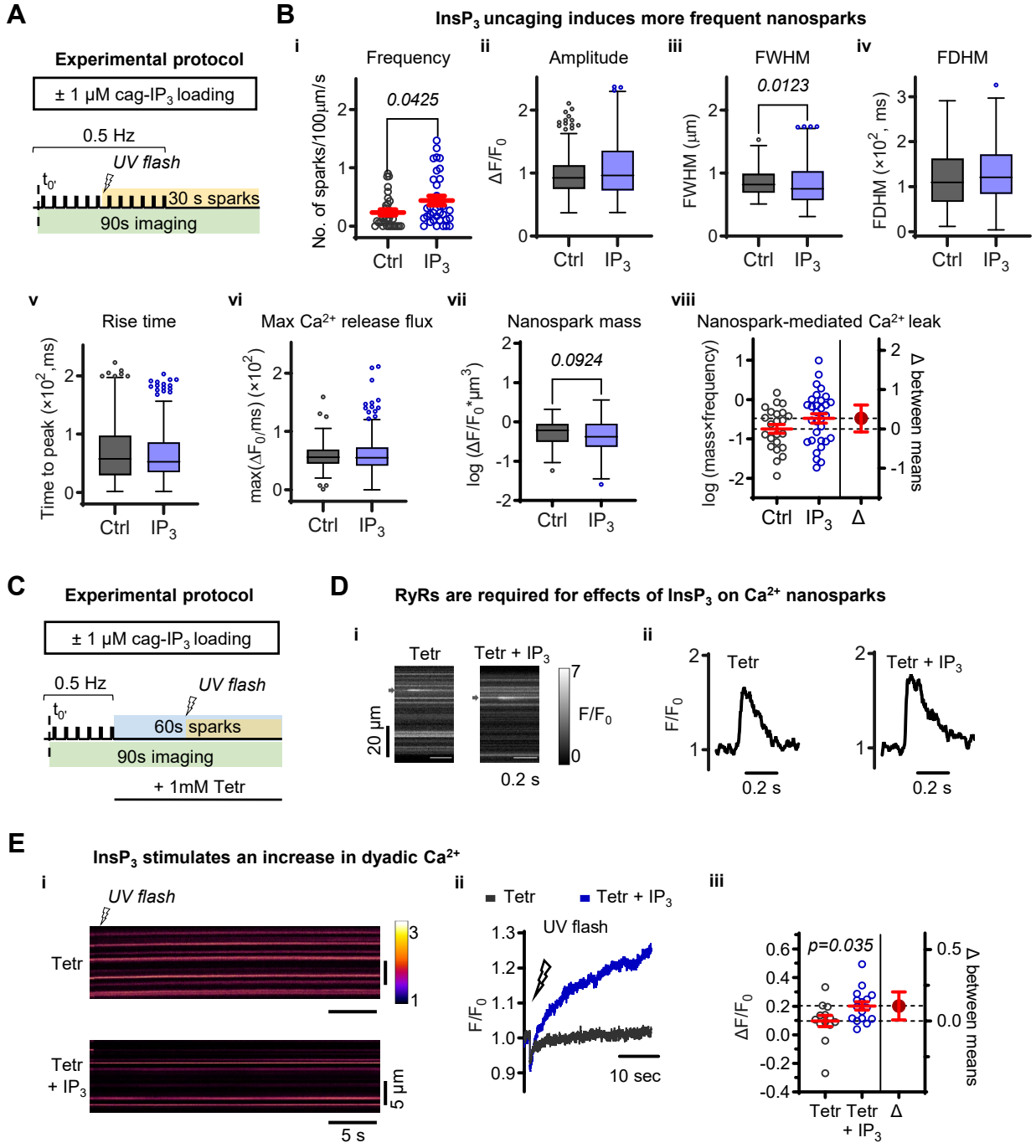
A
Experimental protocol
± 1 µM cag-IP3 loading
0.5 Hz
UV flash
t0'
30 s sparks
90s imaging
B
InsP3 uncaging induces more frequent nanosparks
i
Frequency
No. of sparks/100µm/s
0.0425
Ctrl
IP3
ii
Amplitude
ΔF/F0
iii
FWHM
FWHM (µm)
0.0123
iv
FDHM
FDHM (×10², ms)
v
Rise time
Time to peak (×10², ms)
vi
Max Ca2+ release flux
max(ΔF0/ms) (×10²)
vii
Nanospark mass
log (ΔF/F0*µm³)
0.0924
viii
Nanospark-mediated Ca2+ leak
log (mass×frequency)
Δ
Δ between means
C
Experimental protocol
± 1 µM cag-IP3 loading
0.5 Hz
UV flash
t0'
60s sparks
90s imaging
+ 1mM Tetr
D
RyRs are required for effects of InsP3 on Ca2+ nanosparks
i
Tetr
Tetr + IP3
20 µm
0.2 s
F/F0
ii
Tetr
Tetr + IP3
F/F0
0.2 s
E
InsP3 stimulates an increase in dyadic Ca2+
i
UV flash
Tetr
Tetr + IP3
5 µm
5 s
ii
Tetr
Tetr + IP3
UV flash
F/F0
10 sec
iii
p=0.035
ΔF/F0
Δ between means
Tetr
Tetr + IP3
Δ

Figure 6

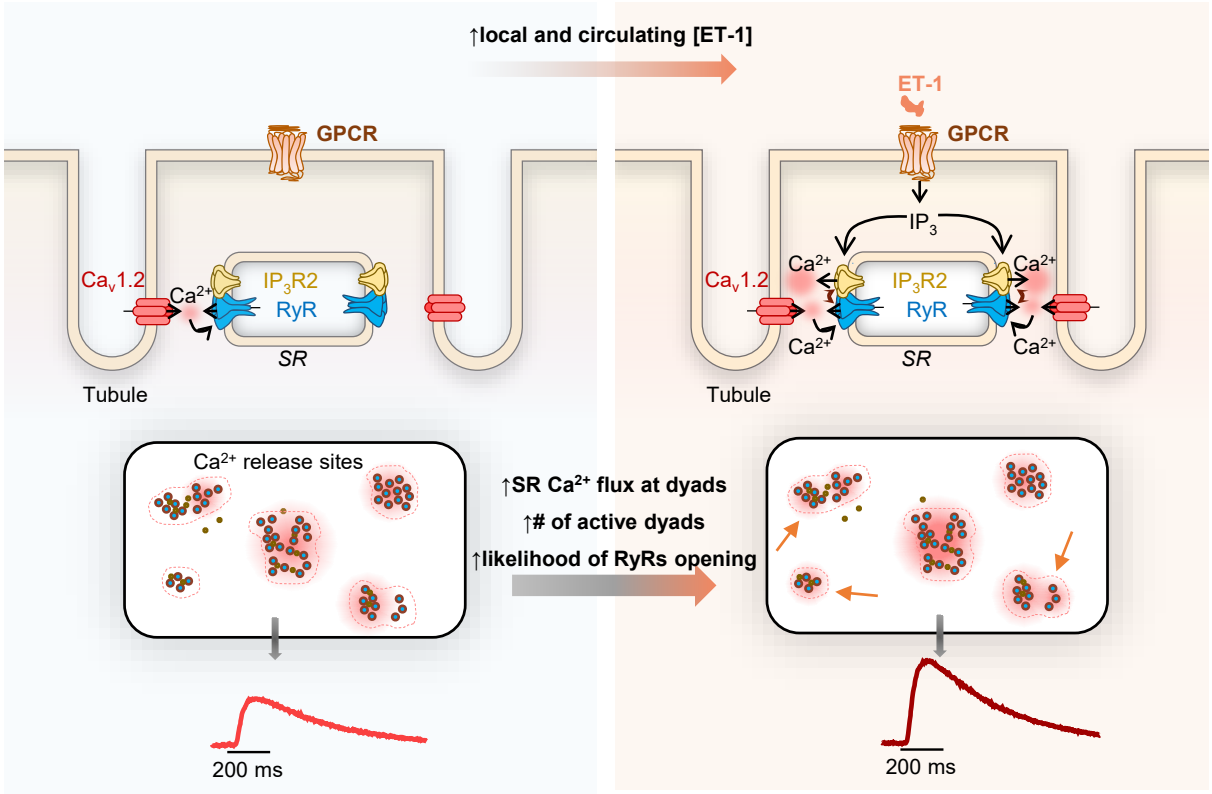
↑local and circulating [ET-1]
ET-1
GPCR
GPCR
IP3
Cav1.2
Ca2+
IP3R2
RyR
SR
Tubule
Cav1.2
Ca2+
IP3R2
RyR
SR
Tubule
Ca2+ release sites
↑SR Ca2+ flux at dyads
↑# of active dyads
↑likelihood of RyRs opening
200 ms
200 ms

Figure 7

Figure S1

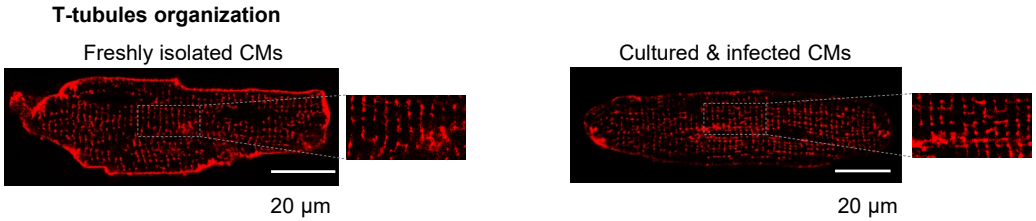

Figure S1. Cardiomyocytes retain the T-tubule network after 48 h in culture

Confocal images of freshly isolated (left) and cultured (right) ventricular cardiomyocytes cardiomyocytes with TTs stained with RH237 are shown. A magnified view of the indicated regions in the images is given to the right.

Figure S2

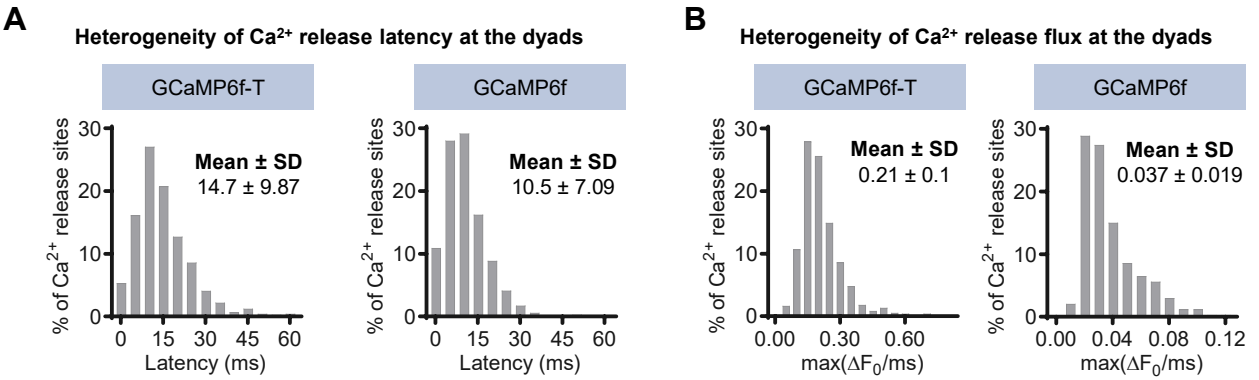

Figure S2. Heterogeneous Ca^{2+} release activation and Ca^{2+} flux at individual dyads were reported by GCaMP6f-triadin and non-targeted GCaMP6f

(A) Frequency distribution histograms of measurements for latency at single release sites recorded with GCaMP6f-triadin (left) and non-targeted GCaMP6f (right). (B) Distribution of measurements max(ΔF_0/ms) recorded with GCaMP6f-triadin (left) and non-targeted GCaMP6f (right) at release sites marked by di-8-ANEPPS labelling. Data from $n_{cells}/N_{animals}$=23/5 for GCaMP6f-triadin and $n_{cells}/N_{animals}$=21/6 for non-targeted GCaMP6f. The number of release sites is 689 and 339 for GCaMP6f-triadin and non-targeted GCaMP6f respectively.

Figure S3

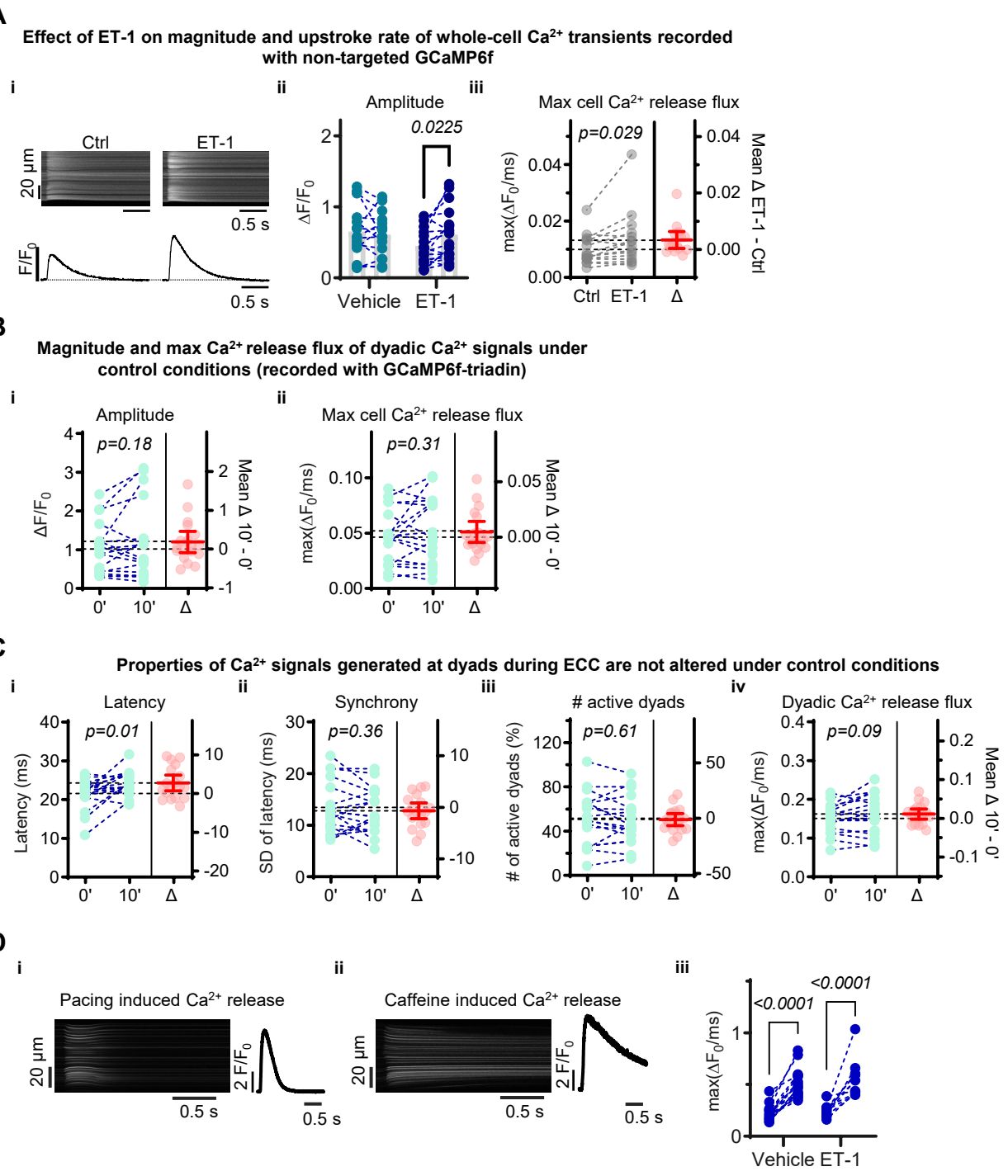
A
Effect of ET-1 on magnitude and upstroke rate of whole-cell Ca2+ transients recorded with non-targeted GCaMP6f
i
ii
iii
Ctrl
ET-1
20 µm
0.5 s
F/F0
Amplitude
0.0225
ΔF/F0
Vehicle
ET-1
Max cell Ca2+ release flux
p=0.029
max(ΔF0/ms)
Mean Δ ET-1 - Ctrl
Ctrl
ET-1
Δ
B
Magnitude and max Ca2+ release flux of dyadic Ca2+ signals under control conditions (recorded with GCaMP6f-triadin)
i
ii
Amplitude
p=0.18
ΔF/F0
Mean Δ 10' - 0'
Max cell Ca2+ release flux
p=0.31
max(ΔF0/ms)
Mean Δ 10' - 0'
0'
10'
Δ
C
Properties of Ca2+ signals generated at dyads during ECC are not altered under control conditions
i
ii
iii
iv
Latency
p=0.01
Latency (ms)
Synchrony
p=0.36
SD of latency (ms)
# active dyads
p=0.61
# of active dyads (%)
Dyadic Ca2+ release flux
p=0.09
max(ΔF0/ms)
Mean Δ 10' - 0'
D
i
ii
iii
Pacing induced Ca2+ release
Caffeine induced Ca2+ release
20 µm
0.5 s
2 F/F0
<0.0001
<0.0001
max(ΔF0/ms)
Vehicle
ET-1

Figure S3. Effect of prolonged pacing, ET-1 and caffeine stimulation on dyadic SR Ca^{2+} release

(A) Quantification of the ET-1 effect on Ca^{2+} transients recorded with non-targeted GCaMP6f. (i) Examples of confocal linescan images (top) and corresponding F/F_0 fluorescence profiles (bottom) before and after 10 min stimulation with ET-1. (ii) Comparison of the magnitude of cell-wide Ca^{2+} transients under control and ET-1 stimulation. (iii) Quantification of Ca^{2+} transient upstroke rate before and after ET-1 treatment. (B) Quantification of peak ($\Delta F/F_0$) (i) and upstroke rate of Ca^{2+} transient ($max(\Delta F_0/ms)$) (ii) recorded with GCaMP6f-triadin during 10 min pacing. (C) Quantitative analysis of spatiotemporal synchrony of SR Ca^{2+} release (i-iii) and maximal Ca^{2+} release fluxes at the dyads (iv) during 10 min pacing under control conditions. Data is presented as repeated measures at start and after 10 min of pacing. Each data point corresponds to the average value of a parameter from a single cell. Data are from $n_{cells}/N_{animals}$: 18/4. A paired t test was used to assess statistically significant differences. (D) Sensitivity of GCaMP6f-triadin to detect relative changes in Ca^{2+} release fluxes induced by caffeine. Examples of confocal linescan images (left) and corresponding F/F_0 profiles (right) of fluorescence changes reported by GCaMP6f-triadin during field stimulation (i) and caffeine application (ii). (iii) Quantification of maximal Ca^{2+} release flux ($max(\Delta F_0/ms)$) during ECC and after caffeine application under control and ET-1 treatment. Mean data are from $n_{cells}/N_{animals}$=11/4 and $n_{cells}/N_{animals}$=18/5 for the ET-1 treated and control groups respectively. The effect of treatment was examined by two-way repeated measures ANOVA with Bonferroni post hoc test.

Figure S4

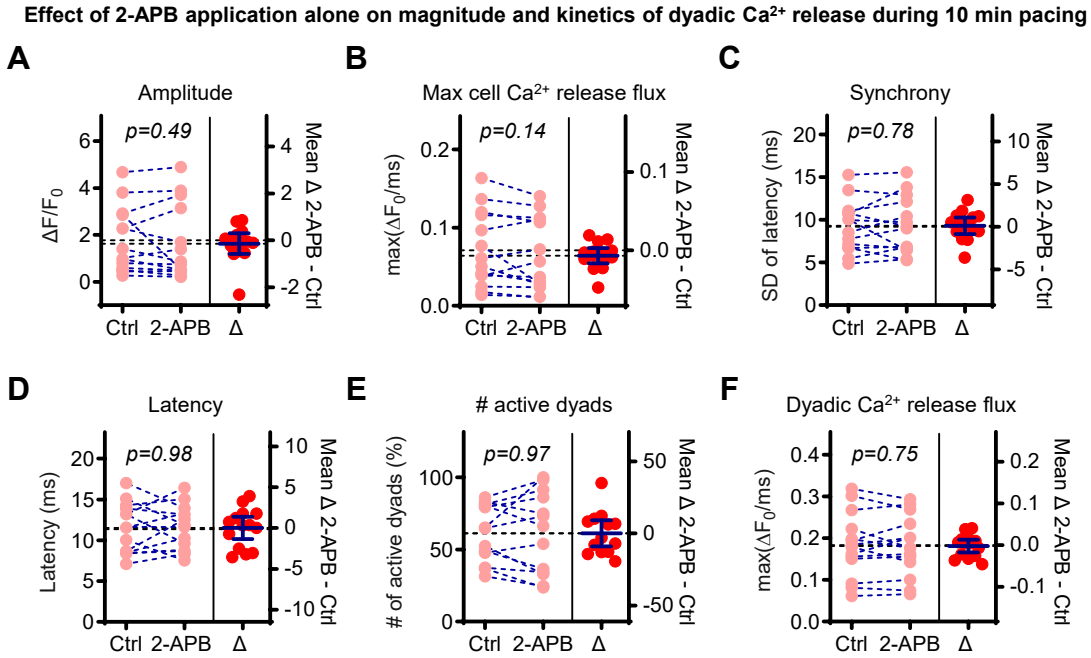

Figure S4. Effect of 2-APB application alone on dyadic Ca^{2+}

(A) Amplitude of whole-cell Ca^{2+} transients ($\Delta F/F_0$). (B) Upstroke rate ($max(\Delta F_0/ms)$) of whole-cell Ca^{2+} transients. (C) Deviation of latency of Ca^{2+} release at individual dyads. (D) latency of Ca^{2+} release onset at individual dyads. (E) Percentage of active release sites. (F) Ca^{2+} release fluxes at individual dyads. Data is presented as repeated measures before and after stimulation. Each data point corresponds to the average value of a parameter from a single cell. Data are from $n_{cells}/N_{animals}$: 14/4 and n of release sites 674/636. A paired t test was used to assess statistically significant differences.